Winter 1-28-2019

An Experimental and Numerical Investigation of Flow Accelerated FLiBe Corrosion

David B. Weitzel

University of New Mexico

Follow this and additional works at: https://digitalrepository.unm.edu/ne_etds

 Part of the Nuclear Engineering Commons, Other Chemistry Commons, Structural Materials Commons, and the Transport Phenomena Commons

David Weitzel

Candidate

Nuclear Engineering

Department

This thesis is approved, and it is acceptable in quality and form for publication:

Approved by the Thesis Committee:

Youho Lee, Chairperson

Anil Prinja

Amir Ali

**AN EXPERIMENTAL AND NUMERICAL INVESTIGATION
OF FLOW ACCELERATED FLIBE CORROSION**

by

DAVID WEITZEL

**BACHELOR OF SCIENCE IN NUCLEAR ENGINEERING
UNIVERSITY OF NEW MEXICO, 2017**

THESIS

Submitted in Partial Fulfillment of the
Requirements for the Degree of

**Master of Science
Nuclear Engineering**

The University of New Mexico
Albuquerque, New Mexico

May, 2019

ACKNOWLEGEMENTS

I would like to acknowledge Dr. Youho Lee for his guidance and direction over the course of our time together. He taught me that no matter how great the work you do is if you can't communicate it to others it profits you little.

I would like to also acknowledge Dr. Amir Ali for his help throughout my work on the flowing FLiBe corrosion project.

I also acknowledge Dr. Anil Prinja for serving on my defense committee.

Lastly, I acknowledge the Department of Energy's NEUP program for funding the research in this thesis.

Thank you, Mom and Dad, your support has made everything possible.

AN EXPERIMENTAL AND NUMERICAL INVESTIGATION OF FLOW ACCELERATED FLIBE CORROSION

By

David Weitzel

B.S. Nuclear Engineering, University of New Mexico, 2017

M.S. Nuclear Engineering, University of New Mexico, 2019

ABSTRACT

Renewed interest in molten salt reactor technology has brought to light the need for a better understanding of FLiBe corrosion. To this end a flowing FLiBe corrosion test loop was designed to test the flow effects of FLiBe corrosion. The loop consists of a pump, melt tank, and stainless-steel tubing assembly that heats the molten salt to high temperatures and circulates it over test specimens. The experiment has been constructed and has completed initial shakedown testing.

To support the flowing FLiBe experiment, a numerical corrosion model that couples FLiBe electrochemistry, solid metal diffusion, and mass transport was implemented. The model has been successfully validated, and initial results indicate that the addition of nickel protective layers to structural metal will greatly reduce FLiBe corrosion.

TABLE OF CONTENTS

LIST OF FIGURES

LIST OF TABLES

Chapter 1: Introduction

1. Background

A. Material Compatibility Issues of Molten Salt Reactors

In recent years there has been renewed interest in molten salt reactors (MSR). MSRs differ from conventional light water reactors in that they use molten salts as the primary coolant instead of water. The primary reason for choosing a molten salt as the primary coolant is to increase the reactor operating temperature which in turn increases the plant's thermodynamic efficiency. Li_2BeF_4 (FLiBe), one proposed coolant salt, is chemically stable at high enough temperatures to be used with a combined Brayton-Rankine power conversion cycle. MSR designs that use high temperature fluoride salts and a pebble fuel form are referred to as Fluoride Salt Hight Temperature Reactors (FHRs). Combined cycle power conversion is notable for having conversion efficiencies as high as 60% compared to the 30-40% typical to a conventional Rankine cycle. This power conversion cycle is used by the current fleet of natural gas plants which are nuclear power's current main market competitor. Using this more efficient power conversion system would allow FHRs to be more market competitive.[1]

Another advantage of a molten salt coolant is that it operates at atmospheric pressure. Existing light water reactors operated at high pressure which in turn increase the cost of structural materials. High pressures also result in violent coolant venting when a breach occurs. On the other hand, a molten salt system operating at atmospheric pressure would have much lower structural strength requirements. All together this means that an FHR would be cheaper to construct than a comparable light water reactor.[1]

The primary drawback to molten salt coolants is the material compatibility issues that arise. Molten salts dissolve alloying elements out of structural materials weakening them. Unlike typical metal corrosion, a protective oxide layer doesn't form during molten salt corrosion. This in turn leads to more aggressive metal corrosion.[2] Molten salt corrosion is affected by a number of different factors including salt temperature, salt temperature gradients, salt chemistry, fluid flow, alloy composition, and alloy microstructure. In order to effectively predict corrosion rates and design an FHR system these assorted factors must be understood and contextualized.

B. Research Objectives and Scope

The objective of the research presented in this thesis is to characterize the effects of FLiBe flow on metal corrosion. Another objective is to demonstrate the corrosion resistance of a proposed bimetallic composite consisting of Nickel-201 and Incoloy 800H. Nickel is known to be resistant to fluoride salt corrosion, thus it is used as a protective layer against FLiBe.[2] A better understanding of flow accelerated FLiBe corrosion is needed to demonstrate the benefits of the composite design. To these ends a flowing FLiBe corrosion loop was designed and constructed to investigate flow accelerated FLiBe corrosion. In addition, a numerical model of flowing FLiBe corrosion was developed to predict the experimental results and construct the theoretical relationship between the various parameters of FLiBe corrosion.

The scope of the research is as follows. The flowing FLiBe corrosion experiment is conducted over the temperature range of 600 to 700 C and under laminar flow conditions. The entirety of the test loop was designed, procured and built during the course of this research. Fabrication of the bimetallic alloy was handled by a research

collaborator. Lastly the numerical model of flow accelerated FLiBe corrosion was researched and developed to support the above-mentioned experimental work.

2. The History of Molten Salt Reactor Coolants

A. Oak Ridge Molten Salt Reactor Program

MSR technology had its birth with the aircraft reactor program that started in 1950. At the time the US Air Force was interested in a nuclear-powered aircraft for long range, long endurance bombing missions against strategic targets in the USSR. The initial salt and material selections for molten salt reactors was done over the course of the program. In 1953 the Aircraft Reactor Experiment (see figure 1-1), a small molten salt reactor, was brought online and ran for several days.[3] The program officially ended in 1956 as interest in an aircraft reactor dropped off due to the development of intercontinental ballistic missiles and long-range jet bombers.

Figure 1-1 Aircraft Reactor Experiment[2]

While on paper the Aircraft Reactor Program ended in 1956, in reality the project team transitioned into commercial reactor development. One of the major changes that occurred early during the civilian reactor program was the introduction of fuel breeding as a design focus in 1959.[3] At the time a major industry concern was the depletion of world uranium resources. At the time breeder reactors were the focus of the Atomic Energy Commission (AEC) and the MSR program was adjusted to accommodate this focus. The Molten Salt Reactor Experiment (MSRE) was proposed to the AEC at the end of 1959. The proposal was accepted, and design work started during the summer of 1960. The reactor consisted of a 1.37 m diameter and 1.62 m high graphite core with a liquid fuel salt. In 1962 construction started, and in 1965 the reactor went critical.[3] Figure 1-2 shows a photograph of the MSRE reactor core.
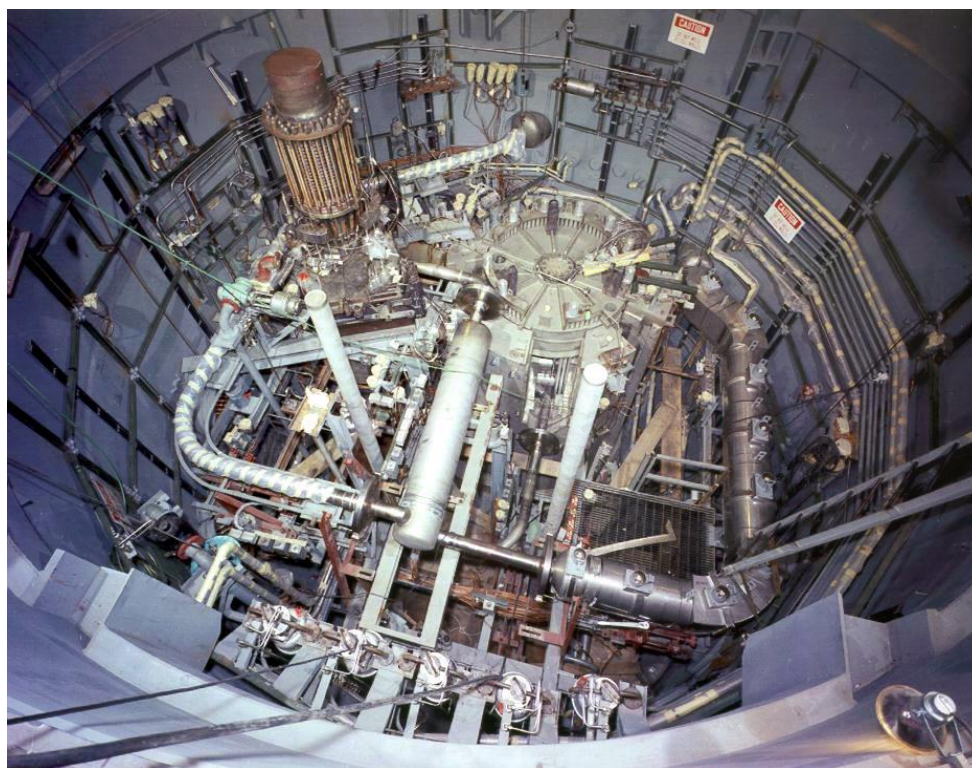
Figure 1-2 Molten Salt Reactor Experiment at Oak Ridge[2]

After a thorough shakedown process, reliable continuous operation was achieved in late 1966. From December 1966 through March 1968 the MSRE operated most of the time conducting various experiments. The reactor fuel was then changed from U-235 to U-233 and ran again from January through May 1969. The MSRE was the first reactor to ever run with U-233. The experiment continued through the end of 1969 and was then ended to transfer funding to other areas within the MSR program. The MSRE experiment produced an invaluable amount of operational data for MSRs and over the course of the experiment many instrumental technologies such as online melt chemistry control, needed for a power reactor were developed. Political support for the MSR program however began to dry up in the seventies which culminated in the cancelation of the program in 1976.[3]

B. Post MSRE Program Research

After the US MSR program was shut down MSR research became sporadic with some industry research and international research in places such as Japan.[3] Fluoride salt research lived on as a prospective fusion reactor breeder blanket.[4] Recent research has primarily taken the form of small scale static material exposure tests and other university lab scale experiments. The fortunes of MSR research however began to change with the generation IV reactor initiative. The new push in MSR technology has been characterized by new design efforts at leading universities as well as the development of new FLiBe purification and testing facilities.[2] A number of new startup companies have started to develop commercial MSR reactors.

C. Modern MSR Designs

One of the leading modern MSR designs is the FHR mentioned earlier in this chapter. The Fluoride Salt High Temperature Reactor (FHR) concept was developed by the University of California, Berkeley, the Massachusetts Institute of Technology, and the University of Wisconsin.[1] The design goals were to address the economic, licensing, and design challenges facing modern MSRs. The key design characteristics of the reactor are as follows.

The FHR is a 236 MWth small modular reactor will pebble fuel form and molten FLiBe as the primary coolant. The FHR was designed to be compatible with existing air-Brayton combined cycle systems used in natural gas plants. The plant is expected to produce 100 MWe when coupled to such an air-Brayton power conversion system. The fuel pebbles are 3.0 cm in diameter and consist of TRISO fuel particles in a graphite matrix. Each pebble contains 1.5 g of uranium fuel. Fuel pebbles are expected to be depleted over 1.4 years and due to the pebble bed design can be continuously replaced. The FLiBe coolant will flow upward through the core with the fuel pebbles floating up with the coolant. The outer pebbles will be inert reflector pebbles. The reactor vessel is 3.5 meters in diameter and 12 meters tall and consists of a graphite reflector and fuel channel for the pebbles. The graphite in the core is the primary tritium sink in the reactor. The FLiBe heated in the core the flows through coiled tube air heaters to transfer the energy into the combined air-Brayton cycle. Figure 1-3 shows a diagram of the FHR reactor core. All together the FHR as described above integrates a number of recent innovations with preexisting MSR technology.[1]
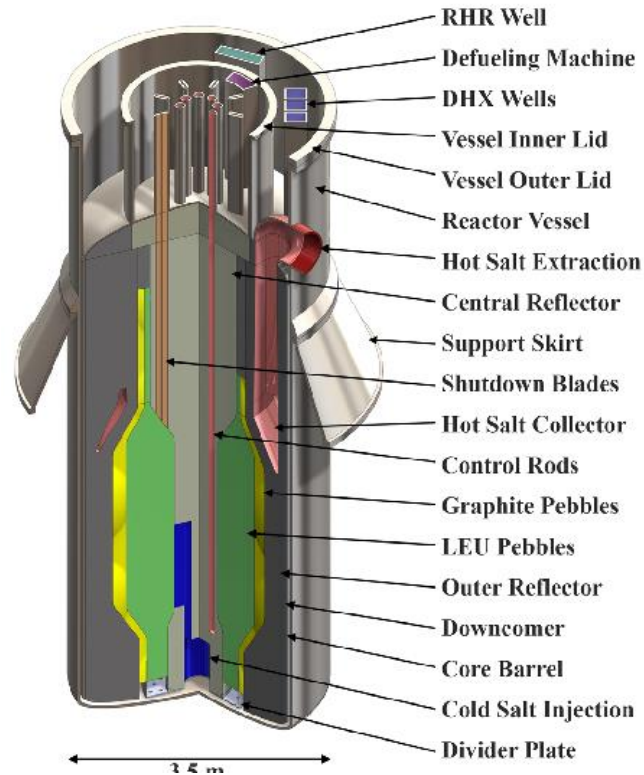
Figure 1-3 FHR Reactor Diagram[1]

One area of lingering concern for the FHR is the issue of structural metal corrosion in FLiBe. While existing research from the MSRE program suggest that corrosion will be within acceptable limits, a better mechanistic understanding of FLiBe corrosion is needed for a more precise material selection and design.

Chapter 2: Principles of FLiBe Corrosion

1. Physical Properties of FLiBe

FLiBe is a eutectic salt mix of 66% LiF and 33% BeF_2. The term FLiBe comes from rearranging the constituent elemental symbols of the salt into an easy to use monosyllable form. FLiBe salt was chosen as a reactor coolant for a number of overlapping reasons including its low impact on neutronics, low viscosity, and low melting point compared to other molten salts.[2] The reason for these advantages comes from the nature of the elements in question.

FLiBe is an excellent material in terms of neutronics. Each of the constituent isotopes with the exception of Li6 have low neutron capture cross sections. Table 2-1 lists the neutron capture cross sections of each of the naturally occurring constituents of FLiBe.

Table 2-1 FLiBe Isotope Neutron Capture Cross Sections

Isotope	Neutron Capture Cross Section
Be^9	8 mb[5]
F^{19}	9.5 mb[5]
Li^7	45 mb[5]
Li^6	941 b (n,α)[5]

Lithium 6 has a large cross section of 941 b for its neutron capture alpha emission reaction; this reaction also produces tritium which is drawback for most industry applications.[5] Fortunately Lithium 6 only represents 7% of natural lithium and can be enriched out to lower the neutron absorption impact of FLiBe. Overall the very low

capture cross sections of the component isotopes of enriched FLiBe make it an excellent reactor coolant from a neutronic stand point.

Moving on to the chemical properties, Lithium Fluoride (LiF) is an ionic compound that disassociates into its component ions upon melting. Beryllium Fluoride (BeF_2) on the other hand doesn't disassociate into ions once melted. This is due to the higher electronegativity of Beryllium. Molten Beryllium Fluoride is a viscous fluid consisting of long glassy chains of nonionic Beryllium Fluoride dipoles.[2] Pure Beryllium Fluoride is too viscous compared to other potential coolants to be useful for reactor applications, but the chemical interaction between Beryllium and Lithium Fluoride overcomes this limitation.

The interaction in question is Lewis Acid and Base chemistry. A Lewis Acid is a molecule with a constituent atom that, while neutrally charged due to its chemical bonds, still has an incomplete valence shell missing an even number of electrons. To complete the valence shell the atom in question accepts one or more free electron pairs from a Lewis Base in a coordinate covalent bond. In a coordinate covalent bond free electron pairs from the Lewis Base associate with the Lewis Acid forming a weak bond. In the case of FLiBe, BeF_2 is a Lewis Acid that forms two coordinate covalent bonds with the Lewis base Fluoride ions to form BeF_4^{2-} as shown in equations 2-1.

$$BeF_2 + 2Li^+ + 2F^- \rightarrow BeF_4^{2-} + 2Li^+ \qquad (2\text{-}1)$$

The coordinate covalent bond isn't strong enough to overcome the ionic bound of solid LiF but can form with the free fluoride ions of a salt melt. BeF_4^{2-} in turn is an ion and thus doesn't form the same glassy chains of BeF_2. As one would expect from equation 2-1, FLiBe has its lowest viscosity (8.6×10^{-3} Pa*s) when the ratio of LiF to BeF_2 is the

stoichiometric two to one.[2] The melting point of 66% LiF FLiBe is 459˚C.[2] FLiBe's

lowest melting point is 356˚C at roughly 50% LiF. The 66% LiF FLiBe mixture selected

for use in reactors was optimized for the lowest viscosity as opposed to the lowest

melting point.

Table 2-2 lists a number of thermophysical properties of FLiBe. Overall FLiBe's

good heat transfer characteristics and its low melting point compared to the intended 600

to 700˚C operating temperature make it an optimal choice for a molten salt reactor

coolant.

Table 2-2 Thermophysical Properties of FLiBe

Melting Point[2]	459°C
Density[6]	$\rho\left(kg/m^3\right) = 2413.03 - 0.4884 * T(K)$
Dynamic Viscosity[6]	$\eta(Pa * s) = 0.000116 * exp\left(\frac{3755}{T(K)}\right)$
Thermal Conductivity[6]	$\lambda = 1.10 \, W/m * K$
Heat Capacitance[6]	$C_p = 2385 \, J/kg * K$

2. FLiBe Corrosion

A. Quantitative Description of FLiBe Corrosion

Metal corrosion in fluoride salts is an irreversible electrochemical reaction that

occurs at the interface of the salt melt and metal.[7] The metal serves as the anode of the

reaction and dissolves into the melt. Oxidants in the salt serve as the cathode and are

reduced. Whether or not the reaction occurs spontaneously depends on the Gibbs free energy of formation. Equation 2-2 show the electrochemical Gibbs free energy equation.

$$\Delta G = -nF\Delta E \qquad (2\text{-}2)$$

ΔG is the Gibbs free energy and has units of J/mol. F is the Faraday constant, 96,485 C/mol. n is the number of charges exchanged in the reaction. Lastly ΔE is the potential difference between the cathode and the anode. If the anode has a smaller potential than the cathode then the reaction occurs spontaneously. In the case of steels an example reaction is the reduction of NiF_2 impurities in the melt (reference potential -2.42 V[7]) and the oxidation of Cr metal at the alloy surface (reference potential -3.28 V[7]) as shown in equation 2-3.

$$Ni^{2+} + Cr \rightarrow Ni + Cr^{2+} \qquad (2\text{-}3)$$

NiF_2 is an impurity of concern in the molten salt while Cr is a common alloying element in structural metals. The expected result of the electrochemical process is the deposition of Ni and the dissolution of Cr into the salt. This reaction weakens the structural metal by removing a key alloying element from the alloy and altering the microstructure at the surface and along the grain boundaries. A more general application of equation 2-2 can be accomplished by looking at a chart of the gibs free energy of formation for metal fluorides such as figure 2-1.
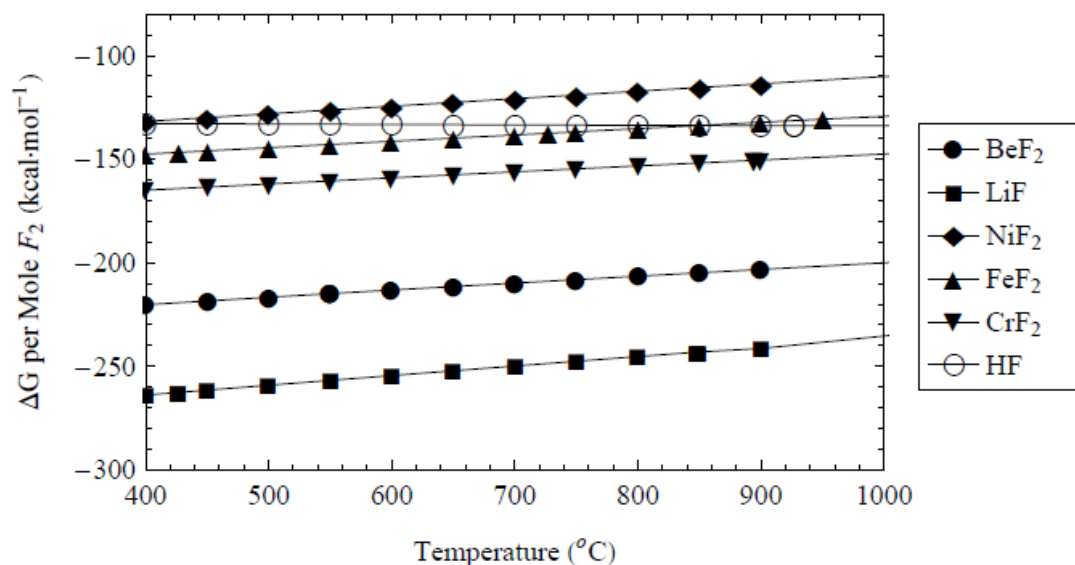
Figure 2-1 Temperature Dependent Gibbs Free Energy of Select Metal Fluorides[2]

Each line in figure 2-1 shows the temperature dependent Gibbs free energy of formation

for a metal fluoride. As explained above metal fluorides will be reduced by metals that

produce fluorides that appear lower on the chart. Conversely metal whose metal fluorides

appear higher on the chart are more resistant to FLiBe corrosion; hence the selection of

nickel for corrosion protective layers. At a glance one can predict that Beryllium metal

would reduce Chromium, Iron, and Nickel Fluorides. Chromium metal, present in most

high-performance steels, would reduce Iron and Nickel Fluorides. Charts such as figure 2-

1 can be compared to structural metal composition and the expected impurities in the

molten salt to predict the corrosion reactions that will occur. The chart can also be used to

select a sacrificial metal to prevent structural alloy corrosion. A typical sacrificial metal is

pure beryllium. As mentioned before beryllium metal reduces structural metal fluorides

and would react with oxidants in the melt before the structural metal did.

So far only corrosion due to structural metal impurities have been discussed. Two other important corrosion pathways are the reduction of actinides and hydrogen fluoride corrosion due to moisture. Actinide corrosion occurs in fuel salts when actinides such as UF_4 are reduced to UF_3. This reduction frees up fluoride ions to react with structural materials accelerating corrosion. Depending on the condition of the salt, this reaction can be a large contributor to the corrosion of a system's metal. Actinide corrosion is primarily a concern in reactors with fuel salts. The FHR design has fuel contained in TRISO particles essentially eliminating actinide corrosion.[1]

Moisture driven corrosion occurs when water molecules react with fluoride ions to produce HF, oxides, and hydroxides as shown in equations 2-4 and 2-5.

$$H_2O + 2F^- \rightarrow O^{2-} + 2HF \tag{2-4}$$

$$H_2O + F^- \rightarrow OH^- + HF \tag{2-5}$$

The oxides and hydroxides react with metal ions and precipitate out of the melt while the HF further oxidizes the structural metal. The above reactions have the net effect of freeing fluoride ions to further corrode the metal in the system. The presence of moisture in the salt melt tends to greatly accelerate structural metal till the water is depleted.[2] This effect is commonly observed in FLiBe corrosion tests as a rapid initial corrosion rate that then drops off.[10]

The electrochemical reduction processes for the reactants described above are governed by the Butler-Volmer equation (equation 2-6).

$$i = i_o \left\{ exp \left[\frac{(1-\alpha)nF}{RT} \eta \right] - exp \left[\frac{-\alpha nF}{RT} \eta \right] \right\} \tag{2-6}$$

Where i is the current density (A/cm^2), i$_o$ is the exchange current density (A/cm^2), α is the charge transfer coefficient, n is the charge of the ion, F is the Faraday constant, R is the gas constant, T is the temperature, and η is the overpotential which equals E$_{electrode}$ − E$_{equilibrium}$. The electrode potential is the potential in the melt while the equilibrium potential is the potential when the reactants are at equilibrium concentrations. Equation 2-7 is used to calculate the equilibrium potential.

$$E_{M^{n+}/M} = E^*_{M^{n+}/M} + \frac{RT}{nF} \ln \frac{C_{M^{n+}}}{C_M} \tag{2-7}$$

E* is the tabulated formal potential. R is the gas constant. T is the temperature. And C is the concentration of metal fluoride in the melt and the solid metal in the alloy. Equation 2-8 is the equation for the exchange current density.

$$i_o = nFk^\circ C_{M(n)}^{b\,1-\alpha} X_M{}^\alpha \tag{2-8}$$

Where k^o is the reaction rate, C is the bulk concentration in the fluid, and X is the concentration in the metal. The corrosion rate is determined by calculating the current density curves with equation 2-6 for each reactant present in the melt. The oxidation and reductions are then summed together for each electrode potential. The correct electrode potential is the one at which the sum of the current densities is zero, or in other words when the oxidation rate matches the reduction rate. This method is capable of factoring as many reactant as required into the calculated corrosion rate.

Once the electrode potential is found, the current density for the corroding structural materials can be converted to species flux by equation 2-9.

$$i = nFJ \tag{2-9}$$

Where J is flux in units of mol/cm^{2}s. The surface flux in this case is the corrosion rate per unit area. The mass loss rate can be derived by multiplying the molar flux by the atomic weight of the corroding metal.

B. Qualitative Description of FLiBe Corrosion

The equations above quantitatively describe the corrosion rate in FLiBe systems. In addition, a number of qualitative effects of FLiBe corrosion can be observed. The most distinctive feature of fluoride corrosion is the absence protective oxide layers at the metal surface. Oxides formed during FLiBe corrosion are soluble in fluoride salts. This results in corrosion products dispersing into melt exposing the metal to further corrosion. The next observation is the tendency for corrosion to occur preferentially along grain boundaries. Figure 2-2 demonstrates gain boundary corrosion from existing FLiBe corrosion literature.
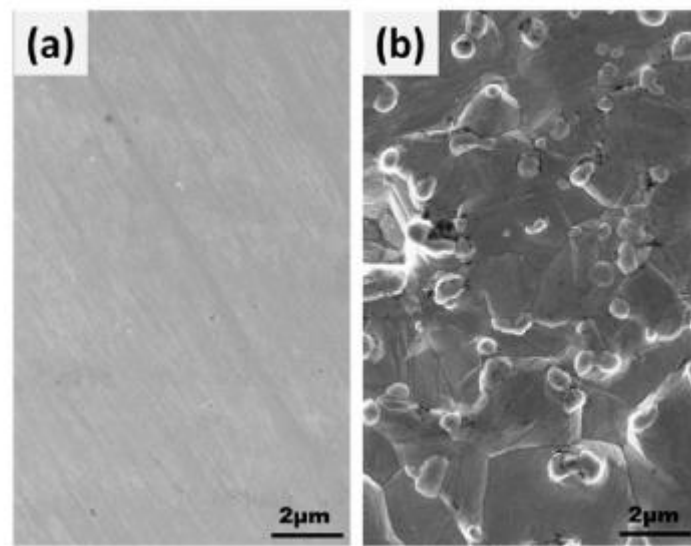
Figure 2-2 a: Pre-corrosion stainless steel b: Post-corrosion steel with preferential grain boundary corrosion[8]

When FLiBe is introduced to a system the most reactive alloying element, typically chromium, reacts with the FLiBe and is depleted from the metal surface. At this point the corrosion would cease unless more chromium becomes available to react with FLiBe at the surface. The depletion of chromium at the surface of the metal creates a chromium concentration gradient that drives solid metal diffusion of chromium to the metal surface. Chromium diffuses faster along grain boundaries than within metal grains.[8] This results in the grain boundaries functioning as express lanes for chromium to reach the surface and react. Because of this, it is expected that materials with finer grain structures will corrode faster in FLiBe than metals with courser grain structures.

All together metal corrosion in FLiBe is a complex prosses that depends on electrochemical equilibrium between the salt, structural material, and any present contaminates. When fluid flow is added to the corrosion system the process becomes even more complex. Because of this complexity, experimental testing is essential to better understanding how all of these factors interact during FLiBe corrosion.

Chapter 3: Experiment Loop Design and Construction

1. Experiment Overview and Requirements

The goal of the flowing FLiBe corrosion experiment is to test the effects of laminar flow on metal corrosion in FLiBe. This entails exposing metal samples to constant flow conditions for 1000 to 3000 hours. By necessity this means that the experiment must be able to maintain a constant flow velocity and temperature for the entirety of a test run with minimal operator oversight. The following is the list of design requirements and constraints for the corrosion test loop.

The first major constraint is the availability of FLiBe. FLiBe must be specially prepared at Oak Ridge National Laboratory and is only available in small quantities. Thus, a key design constraint is that the loop must be able to run with 1.2 liters or less of FLiBe in the system. The second design requirement is that the loop must produce Reynolds Numbers of up to 2300, the limit of laminar flow, in the system. Third the experiment must be able to independently control temperature and flow rate so as not to have a temperature gradient that affects the corrosion rate. Lastly, due to safety concerns with handling beryllium and fluoride salts the whole facility must be contained to prevent exposure to the operator and others in the laboratory. Together these four requirements drive the experimental design.

2. Loop Engineering Design

At the very start of the design process the need to independently control temperature and flow rate ruled out a convection loop for the experiment, so from the start a forced convection loop with a pump was decided on. Additionally, it was decided that the entire experiment would be contained within a glovebox to prevent outside

exposure to beryllium. As an added bonus, the glovebox would also allow for precise control of the oxygen and water levels within the experiment. With the third and fourth design requirements resolved, the design process continued on the basis of minimizing the system volume and reaching the desired flow conditions.

A. Loop Dimensions Selection

At this point in the design process the two remaining design drivers were the volume limit and the need to provide adequate fluid flow. Figure 3-1 outlines the design process used for the loop.
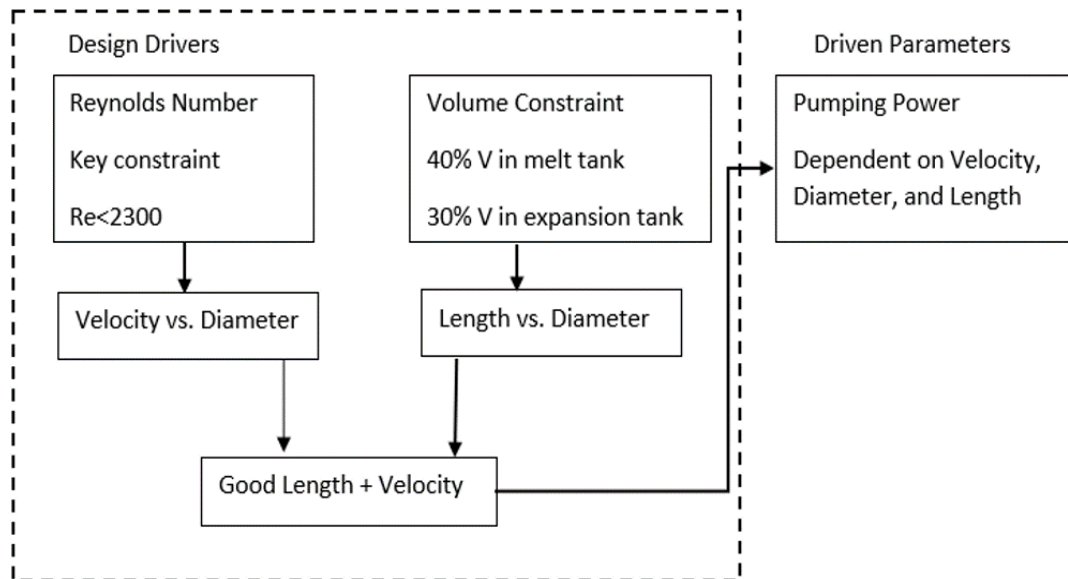
Figure 3-1 Design Process Flow Chart

The common design element between the two design drivers was what diameter of the loop tubing. The purpose of the test loop is to replicate the flow conditions found in a MSR. For the design, laminar flow is sought at Reynolds numbers under 2300. The well known equation for the Reynolds number is as follows:

$$Re = \frac{\rho V D}{\mu}$$

Where Re is the Reynolds number. ρ is the density. V is the fluid velocity. D is the characteristic diameter. And lastly μ is the viscosity. For the fluid flow analysis the temperature dependent density and viscosity were found in literature and are shown in equations 3-1 and 3-2.[5]

$$\rho\left(\frac{kg}{m^3}\right) = 2413.03 - 0.4884 * T(K) \tag{3-1}$$

$$\mu(Pa * s) = 0.000116 * e^{\left(\frac{3755}{T(K)}\right)} \tag{3-2}$$

For the purpose of the preliminary design an operating temperature of 650°C or 923K was selected.

The first step in selecting a tubing diameter was calculating the relationship between flowrate, pipe diameter and Reynolds number. Figure 3-2 shows flow rate in different diameter pipes while Re is held constant. As one would expect flow rate drops as the pipe diameter increases and as Re decreases.
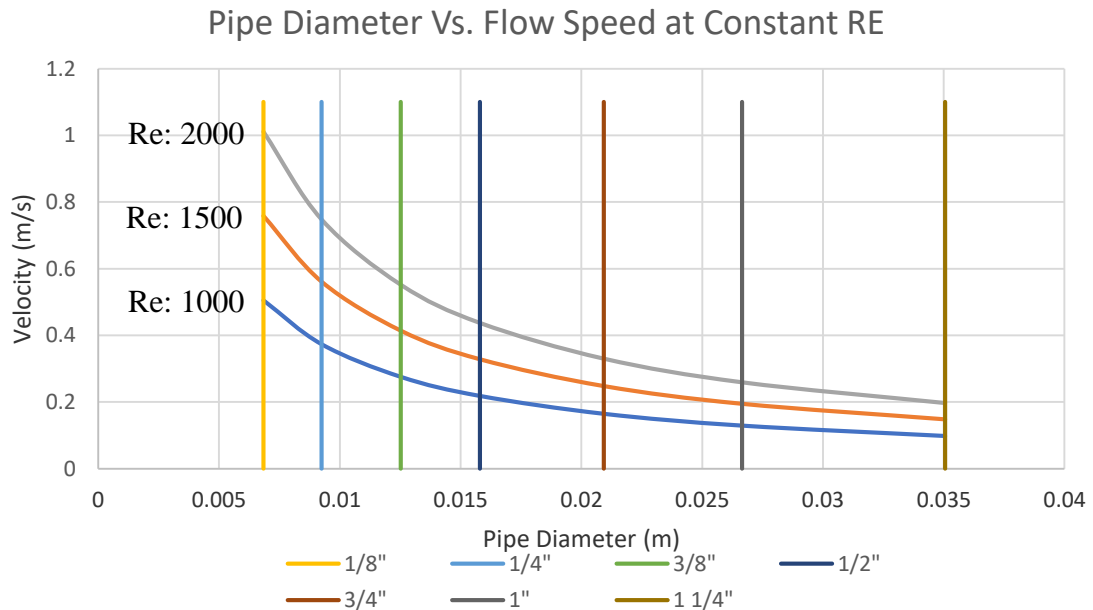
Figure 3-2 Relationship between fluid velocity and pipe diameter at constant Re

Next while deciding on the appropriate system length special attention had to be placed

on the overall system volume. The test loop consists of a melt tank with a pump which

pushes the FLiBe through the test loop. The preliminary design assumed that 40% of the

total volume of FLiBe in the system would be in the melt tank while the loop is operating

to prime the pump. The next step for sizing the system was to calculate the maximum

tubing length for each pipe diameter that resulted in 0.7 L (60% of 1.2 L) of FLiBE in the

loop. Figure 3-3 shows the maximum length of pipe of various diameters that can be

filled with the allotted FLiBe volume. US industry standard pipe diameters are indicated

on the chart for reference. For the design it was decided that at least one meter of loop

length was needed to accommodate the samples and other instrumentation. Based on the

calculated results, tubing one inch in diameter or less would work.
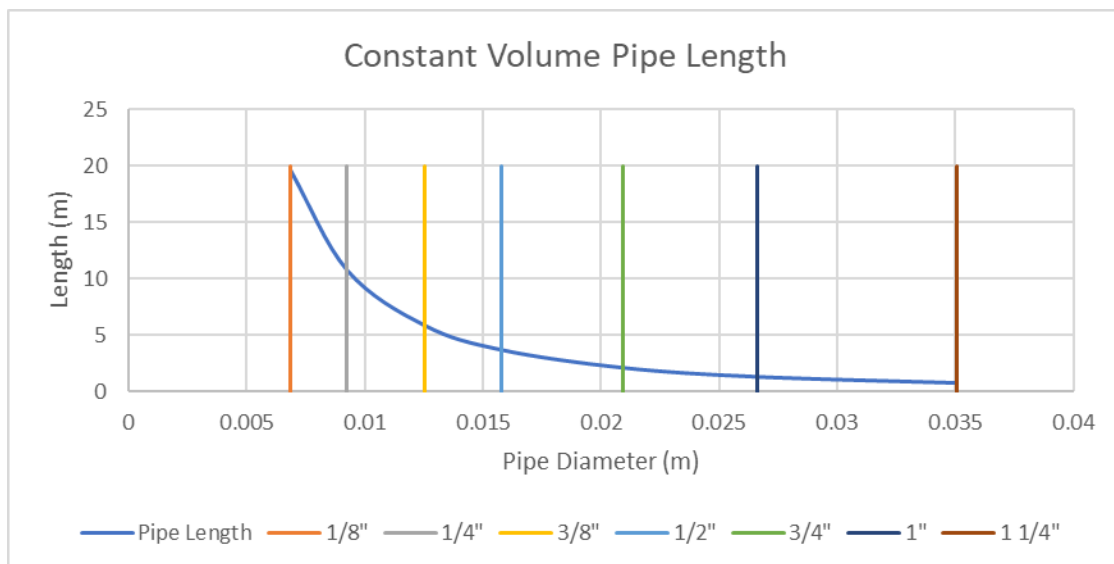
Figure 3-3 Constant Volume Pipe Length

The last sizing parameter to be considered was the pumping power needed for the system.

Equations 3-3, 3-4, and 3-5 were used to derive the pumping power.

$$h_L = (32/Re)(L/D)(v^2/g) \qquad (3-3)$$

Where h_L is pumping head from pipe length. Re is the Reynolds number. L is the tubing length. D is the characteristic diameter. V is the flow velocity. And lastly g is the gravitational acceleration.

$$h_{Lfitting} = \Sigma K(v^2/2g) \tag{3-4}$$

Where $h_{Lfitting}$ is the fitting friction head. K is the resistance coefficient for the fittings. V is the flow velocity. And g is the gravitational acceleration.

$$W = \dot{m}g(h + (h_L + h_{Lfitting})) \tag{3-5}$$

Where W is the pumping power. $\dot{m}$ is the mass flow rate. g is the gravitational acceleration. h is the elevation head. h_L and $h_{Lfitting}$ are the pipe length and fitting friction head.

With these equations the pumping power need for the loop design was calculated. The results of this calculation are shown in figures 3-4 and 3-5. The results assume a 60% pump efficiency and 90% motor efficiency. From the figures it should be noted that even in the worst-case scenario the loop needs less than three watts of pumping power to operate under laminar conditions, so it was deemed that pumping power was unlikely to be the limiting parameter. Ultimately a ½ horsepower (373 watt) motor was ordered to power the pump well exceeding the minimum power requirements.
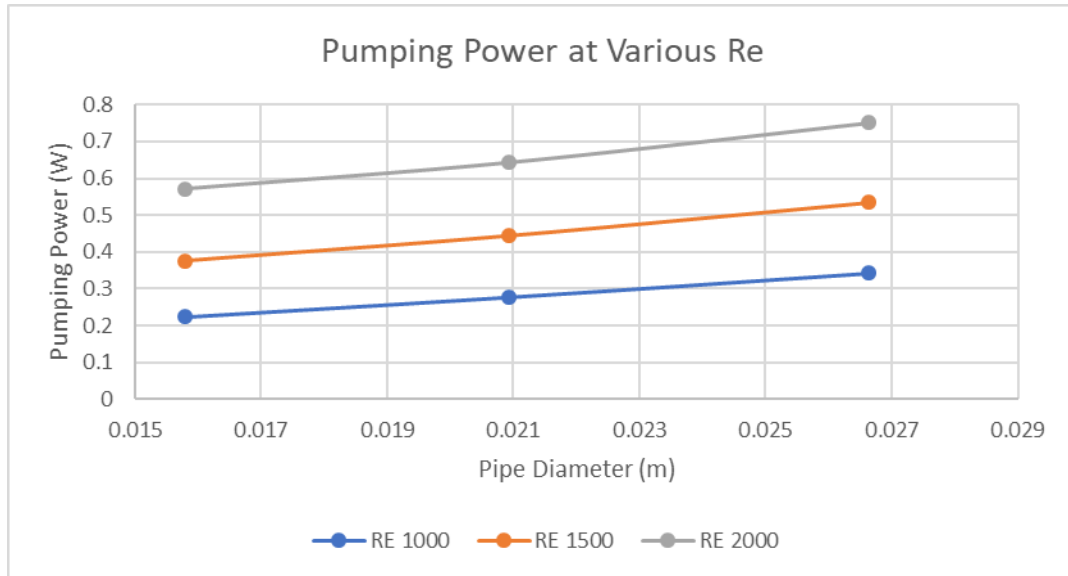
Figure 3-4 Diameter dependent pumping power at various Reynolds numbers
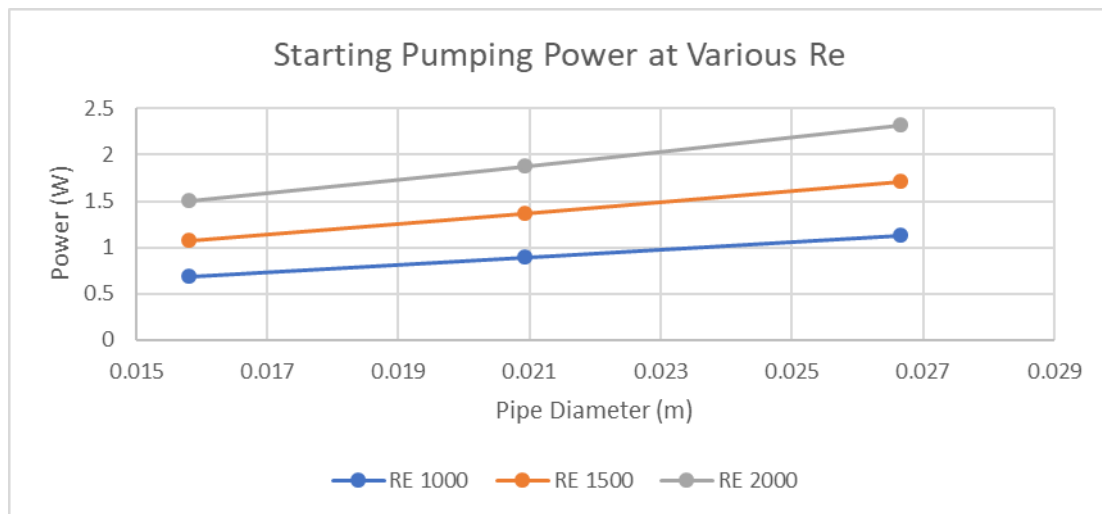
Figure 3-5 Diameter dependent starting pumping power at various Reynolds numbers

After completing all of the above calculations and consulting with the tubing supplier, the

pipe diameter of 3/4 inches was selected. The associated length limits and needed

pumping power were used for selecting and designing the loop components.

B. Loop Component Description

      Figure 3-6 shows the model of the loop with all of its components listed. Table 3-1 outlines the key specifications of the experiment loop. This section describes the design for each component in detail.

1: Flow Meter
2: Expansion Tank
3: Pump
4: Melt Tank
5: Electrodes
6: Thermocouples
7: Tubing
8: Fittings
9: Heating Tape
10: Sample Holder
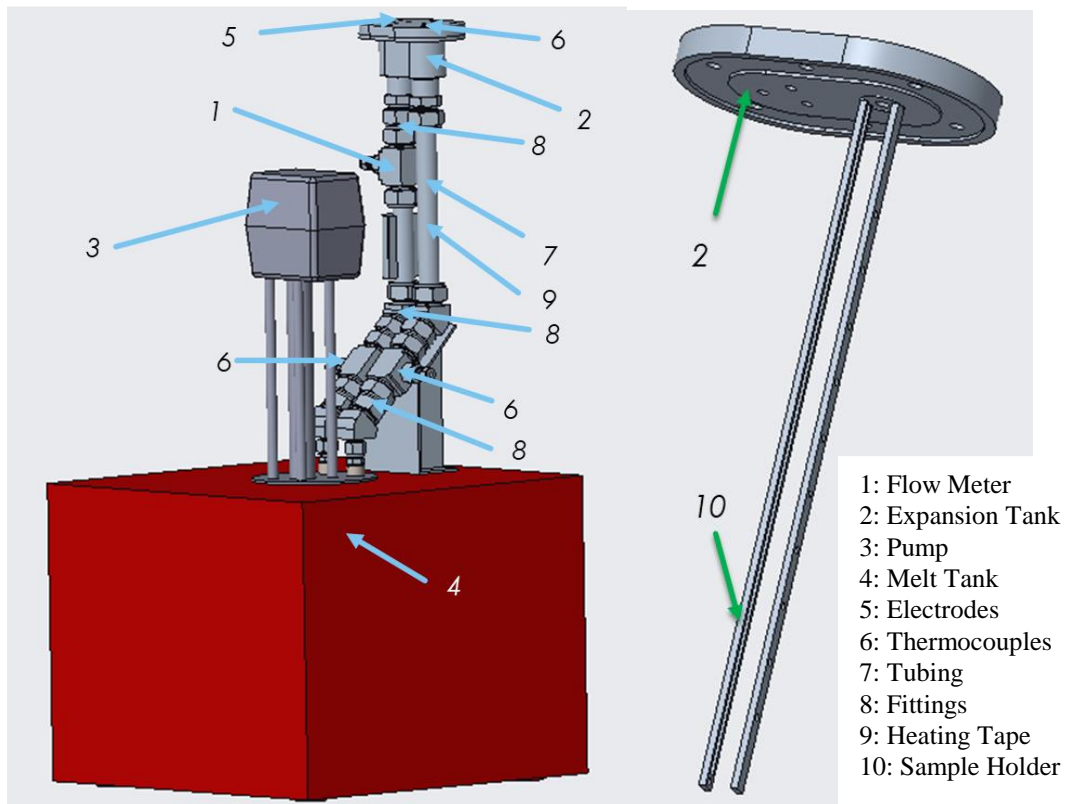
Figure 3-6 Flowing FLiBe corrosion experiment loop

Table 3-1 FLiBe Loop Specifications

Operating Temperature	700 ˚C
Loop Length	36"
System Height	36"
System Foot Print	18" x 18"
Operating Volume	1.2 L
Operating Reynolds Number	500-2000
Instrumentation	3 x thermocouples
	3 x electrodes
	1 x flowmeter

a. Flow Meter

The goal of the flowing FLiBe corrosion test loop is to measure the effect of fluid flow on metal corrosion in a molten salt environment. To this end the flow conditions in the loop must be known so that the flow rate and the corrosion rate can be correlated. Thus, a flow meter was included in the loop to directly the fluid flow. When looking for a flow meter suited for the system, a problem arose. Currently there are no flow meters on the market that are both capable of operating at 700 ˚C and small enough to be connected to the loop. Available high temperature flow meters are designed to be included in large industrial processes and are therefore too large to be included in the loop without dramatically increasing its size and volume. Due to the test run FLiBe volume limit this was not possible. The solution to this problem was to calibrate the pump with a water flow meter and a water shakedown test. The flow meter is used during the initial water

shake down test to measure the correlation between pump controller frequency and the

flow rate. The water flow meter was used during the initial shakedown and then removed

for the molten salt tests.

The flow meter used for the experiment is an Omega FTB-1400 flow meter with a

FLSC-C3-LIQ signal conditioner. The flow meter is shown in figure 3-7.

Figure 3-7 Omega FTB-1400 flow meter with signal conditioner

The flow meter outputs the flow rate as an analog current signal proportional to the

volumetric flow rate. This signal is logged by the experiment's LabVIEW program.

b. Expansion Tank

The expansion tank consists of three parts: the tank itself, the lid, and the gasket

between the tank and lid. The expansion tank is located at the top of the loop and was

designed to address several experimental needs. It is the primary point of access to the

interior of the loop. The experiment samples are load through the expansion tank and

mounted to the expansion tank lid by a threaded holder. The lid is also ported for a thermocouple and three electrodes. All voltammetric analysis will be performed in the expansion tank.

The expansion tank is constructed out of 316 stainless-steel. To protect the stainless-steel from FLiBe corrosion, the interior of the expansion tank will be electroplated with nickel before used in FLiBe corrosion experiments. The body of the tank and the tank lid were machined at UNM by the mechanical engineering department machine shop. The tank is 2" tall, 2" wide, and is 3 ¾" long. The tank also has a 5 5/8" by 3 7/8" flange. Welded to the tank are two Swagelok 1" weld fittings for connecting the expansion tank to the loop itself. The tank lid is ½" thick and is 5 5/8" by 3 7/8" like the tank flange. The lid has one thermocouple and three electrode ports. The thermocouple port consists of a SS316 Swagelok ¼" bore-through fitting. On the interior of the lid the threaded sample holder mount is concentric with the thermocouple port. The electrode ports consist of three SS316 Swagelok 1/8" bore-through fittings. The expansion tank gasket was manufactured at Hennig Gasket company and was made from Pyro-Tex sheet. Pyro-Tex is a high temperature gasket material made of woven stainless-steel leaf spring sheathed in graphite. The gasket material was selected because it is rated for up to 1000˚C operations, and graphite is inert when exposed to FLiBe. Figures 3-8, 3-9, and 3-10 are pictures of the expansion tank, the ported lid, and the Pyro-Tex gasket respectively. The picture of ported lid was taken after the high temperature molten salt shakedown hence the discoloration and debris.

Figure 3-8 Expansion Tank

Figure 3-9 Ported Expansion Tank Lid

Figure 3-10 Pyro-Tex Expansion Tank Gasket

c. Pump and Melt Tank

Conducting the flowing FLiBe corrosion experiment requires a heating system to melt the salt and a pump to push the fluid through the loop. These functions are combined in the integrated pump and melt tank. The pump and melt tank were designed and constructed by Wenesco Inc. to the specifications required for the loop.

The melt tank is 6" in diameter, 7" deep, and constructed from 316 stainless-steel. The melt tank is contained within a 20" x 20" x 15" housing with an integrated 7000W heater. The melt tank is capable of heating its contents to over $700\degree C$ and is controlled by the connected control box. A nickel 201 pot liner will be installed to protect the melt tank from corrosion during FLiBe testing.

The pump is a centrifugal design constructed with a SS316 impeller and housing. The pump impeller assembly fits within the melt tank in order to draw in the melt for pumping. The pump is powered by a ½ horsepower electric motor with a VFD controller housed in the control box. The pump is rated for 0.15 gpm at 5 ft of pumping head; this

converts to roughly .141 W of power. Figure 3-11 shows the pump and melt tank with the

rest of the loop installed.

Figure 3-11 Pump and Melt Tank

The pump is mounted to the 16" diameter melt tank lid. The lid has four 3/8" NPT ports

and one ½" NPT sampling port. Two of 3/8" ports serve as the pump outlet and return

ports. Figure 3-12 shows the layout of the various melt tank lid ports.
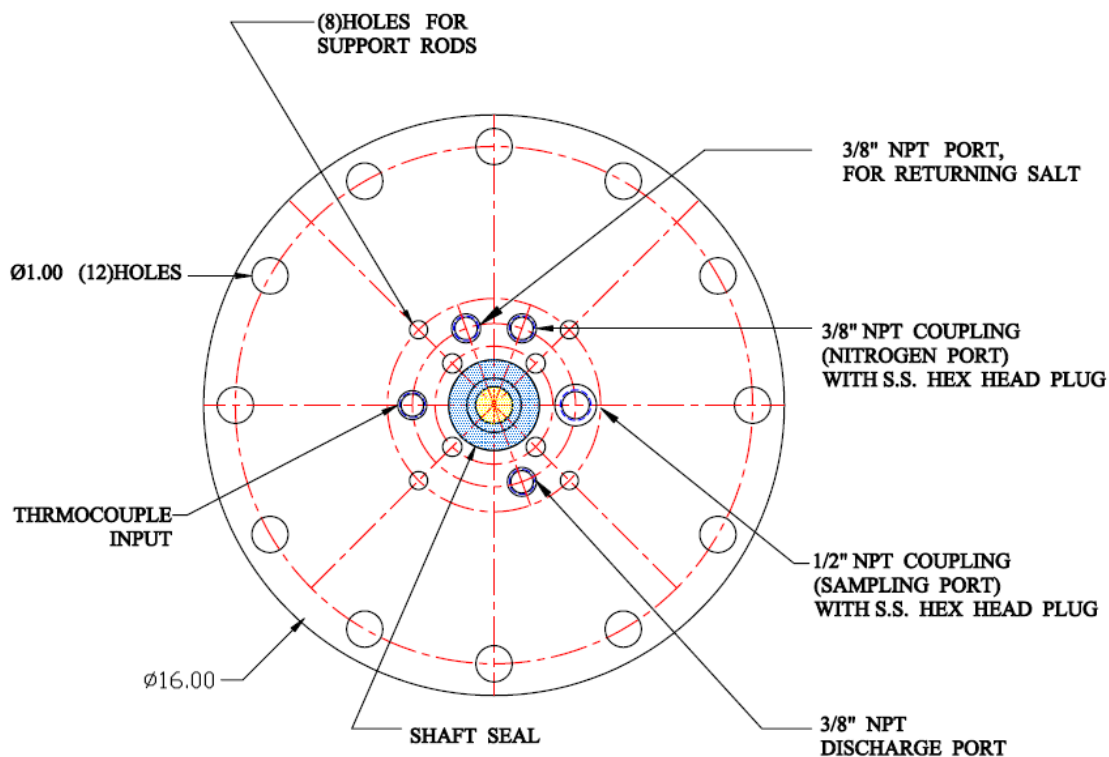
Figure 3-12 Melt Tank Lid Port Layout

d. Electrodes

The use of voltammetric analysis to characterize molten salt corrosion was first demonstrated in the seventies during the MSR program.[10] Voltammetric directly measures the amount of impurities in the salt. During voltammetric analysis a series of electric potential are applied to the solution. As the potential becomes large enough to separate the components of a metal fluoride the current increases as salt constituents move towards the anode and cathode. By noting the voltages and current the species and quantity of impurities in the melt can be measured. Voltammetric analysis allows for continuously observing the change of salt composition during the experiment. This in turn will allow for correlating the corrosion rate with the salt composition. More recent work done in the Czech Republic demonstrated a nickel, tungsten, and glassy carbon

three electrode effectively measured the voltammetry in FLiBe.[9] will be used to preform

electrochemical analysis on the FLiBe during operations. For the FLiBe corrosion test

loop 1/8" nickel, tungsten, and glassy carbon electrode rods are installed through the

expansion tank lid to perform voltammetric analysis during the experiment. The

voltammetric analysis will be controlled by a digital power supply connected to the

experiment's LabVIEW software.

e. Thermocouples

The flowing FLiBe corrosion experiment aims to determine the effects on

corrosion of isothermal flow. Thermocouples are needed to measure the salt temperature

throughout the loop. Because of the high temperatures and exposure to corrosive FLiBe a

robust thermocouple was needed. For this reason ¼" diameter 6" long Omegaclad K-type

thermocouples manufactures by Omega were selected for use with the experiment. The

large size and the nickel-based shaft alloy will protect the thermocouples during high

temperature operations in FLiBe. There are three thermocouples installed throughout the

loop. Two are installed next to the pump outlet and return and the third is installed in the

expansion tank lid to measure the temperature of the salt exiting the test section. Figure 3-

13 is a picture of the selected thermocouples.

Figure 3-13 ¼" Diameter Omegaclad K-type thermocouple

d. Tubing and Swagelok Fittings

The loop itself is constructed from 1" OD ¾" ID stainless steel tubing and stainless-steel Swagelok fittings. Eventually the stainless-steel tubing will be replaced with a Nickel 201/ Inconel 800H bimetallic alloy tubing of the same dimensions for the FLiBe testing. The tubing and fittings are rigid enough for the loop to be self-supporting. There are six tubing sections used in the loop each cut to size in the lab. Two 13" upright tubes are located between the pump connecting fittings and the expansion tank. The pump outlet side upright is the test section of the experiment. Samples mounted in the sample holder are suspended in this section and exposed to the fluid flow. The overall length of this section was selected to allow for the flow to stabilize after the fitting transition and accommodate multiple experiment samples. The remaining four tubes are 2.5" connector sections for joining 1" Swagelok fittings to each other.

The Swagelok fittings serve to connect the loop to the pump, act as instrument ports, and offset the loop from the pump motor assembly. Swagelok fittings were selected for their ease of installation and the familiarity that those involved in the design had with them from other projects. The fittings form two distinct groups. The weld fittings were welded to the expansion tank and lid for loop connections and instrument ports. All the other fittings were used together to transition from the pumps 3/8" NPT fittings to the uprights. These fittings include a 45-degree section to offset the loop from the pump motor assembly. They also include two ports for thermocouples. Table 3-2 lists all the Swagelok fittings used in the loop. The transition assembly fittings are listed in assembly order from the pump to the uprights. Before the FLiBe testing, all stainless-steel loop

components will be nickel plated to protect against FLiBe corrosion. Lastly figure 3-14

provides a picture of the assembled tubing and fittings.

Table 3-2 List of Swagelok Fittings

Quantity	Type
Expansion Tank Fittings	
2	1" Male Weld Fitting
1	¼" Male Weld Fitting
3	1/8" Male Weld Fitting
Pump to Upright Transition Assembly	
2	3/8" to ½" Male Tube adaptor
2	½" 90˚ Union Elbow
2	½" Socket Connector
2	½" 45˚ Union Elbow
2	½" to 1" Reducer
2	1" to ½" Reducing Tee Union
2	¼" to ½" Reducer
2	1" 45˚ Union Elbow
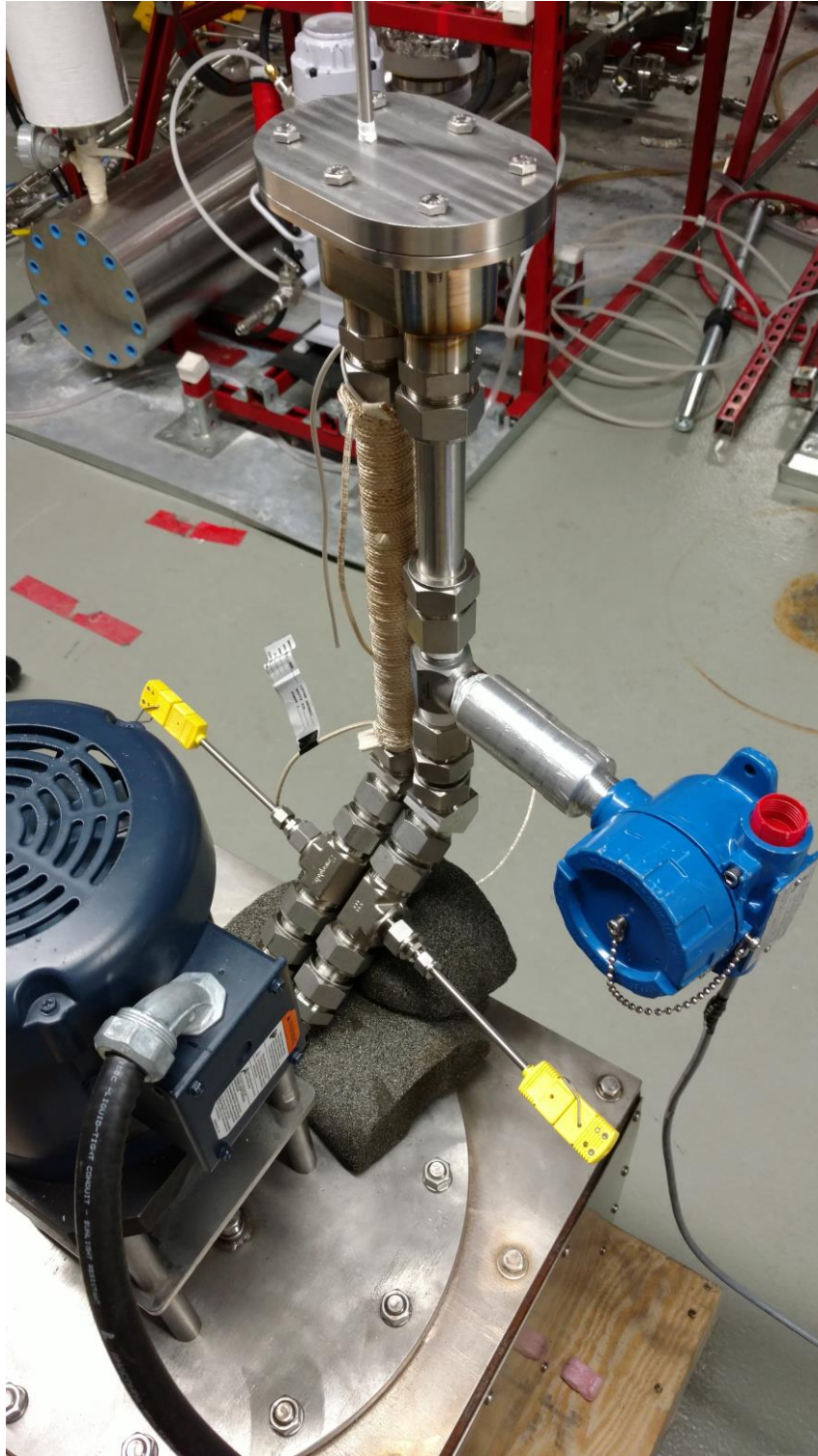
Figure 3-14 Loop of Assembled Tubing and Fittings

e. Heating Tape and Insolation

It is of special concern that the temperature in the test section of the loop be maintained at a constant temperature. To this end a heating tape is mounted around the test section of the loop to maintain a constant salt temperature around the samples. The heating tape is an ultra-high temperature ½" by 2' tape from Omega that is rated up to 1400˚F or 760˚C which is above the 700˚C operating temperature. The heating tape is controlled by the LabVIEW software. The heating tape can be seen installed around the sample section in figure 3-11. In addition to the heating tape, the entirety of the experiment loop is wrapped in Lynn Manufacturing Superwool insolation to reduce heat loss to the surrounding atmosphere.

f. Sample Holder

The sample holder is mounted to the expansion tank lid and is designed to hold the material samples being tested. The sample holder is a foot long and has space for nine samples. The holder consists of two separate slotted brackets joined by a segment of 1/8" rod. The sample holder is designed for 1" x .565" x .125" samples. The holder and samples were manufactured at the UNM mechanical engineering machine shop. The sample holder fits snuggly in the ¾" tubing to prevent the holder from vibrating during testing. Over the course of the experiment samples will removed one at a time for post experiment characterization. Each sample will become a snap shot of the material microstructure at the time of removal. The lowest sample in the holder will also be subjected to the boundary layer evolution allowing for analysis of the effect of boundary layer thickness on corrosion in a single sample. The leading edge of the samples and sample holder was modeled with CFD software to select a holder design that minimized

the sample holder's impact on leading edge's flow profile. Figure 3-15 is a picture of the

completed sample holder mounted to the expansion tank lid. Figure 3-16 shows the CFD

results for the sample holder leading edge.

Figure 3-15 Sample holder with samples
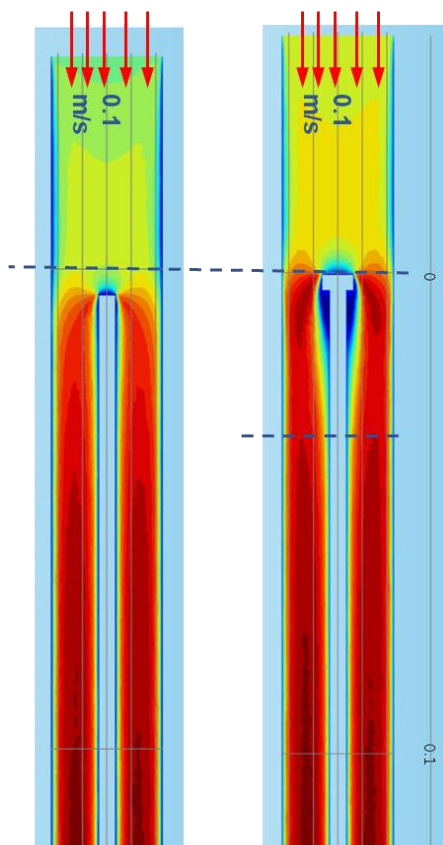
Figure 3-16 CFD model of sample holder

g. Glovebox

In order to protect the experiment operator from beryllium exposure as well as to prevent contaminating the lab space, a glovebox for the loop was ordered from Vigor Tech. The glovebox is filled with an inert atmosphere of argon. The argon atmosphere prevents the introduction of oxygen and water moisture as corrosion agents to the FLiBe. The internal atmosphere conditions are monitored by a moister and an oxygen sensor. The glovebox has a sophisticated purification system that actively removes oxygen and water vapor from the glovebox. The purification system also includes HEPA filters that capture any beryllium particulate released into the glovebox. Two airlocks are included to allow for moving materials into and out of the glovebox without introducing outside air. Work

in the glovebox is conducted using the two sets of gloves in the front windows. The

glovebox has a built-in air conditioner to remove heat given off by the experiment. Figure

3-17 shows a CAD model of the glovebox.
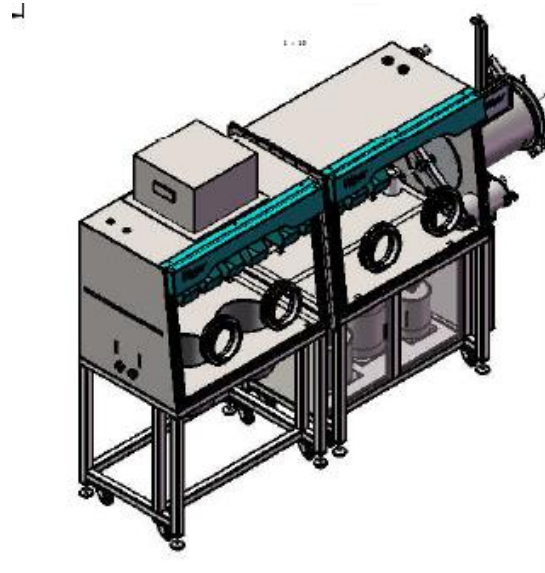
Figure 3-17 Glovebox Model

The glovebox also has a well for the melt tank. The well is sized to allow for mounting

the melt tank below the glovebox floor. To operate electrical equipment and sensors

inside the glovebox, specially designed feedthroughs are connected to the various power

lines. The glovebox feedthroughs are as follows:

- Feedthrough for melt tank electrical lines

- Feedthrough for pump electrical lines

- Feedthrough for electrochemical lines

- Feedthrough for glovebox power strip

- Feedthrough for thermocouple lines

- Gas feedthrough for pressurized argon line

3. Loop Construction

The construction of the experiment began with ordering the pump and melt tank as well as the glovebox from their respective manufacturers. Next the expansion tank and sample holder were ordered from the machine shop. The remaining components mentioned above were also ordered at that time. A new 40A 240V outlet for the pump and melt-tank was installed in the lab by UNM facilities. Assembly of the loop began with the delivery of the pump and melt tank from the manufacturer. At this point the fittings, tubing and instrumentation were put together. The first change made to the loop was the addition of two ½" 90-degree elbow fittings. The new fittings were need for the loop to clear the pump mounting structure. Figure 3-18 shows pictures of the assembled loop as well as pictures of the loops various components.

Figure 3-18 FLiBe loop and component pictures

With the loop assembled an outside contractor was brought in to program the LabVIEW

program for the experiment. The LabVIEW software manages the flow meter, electrodes,

heating tape, and thermocouples. The software logs the data from all of those instruments

as well. The software will be used to monitor and manage the test loop for the entirety of

the months long experiment runs. Figure 3-19 shows the interface for the LabVIEW

software.
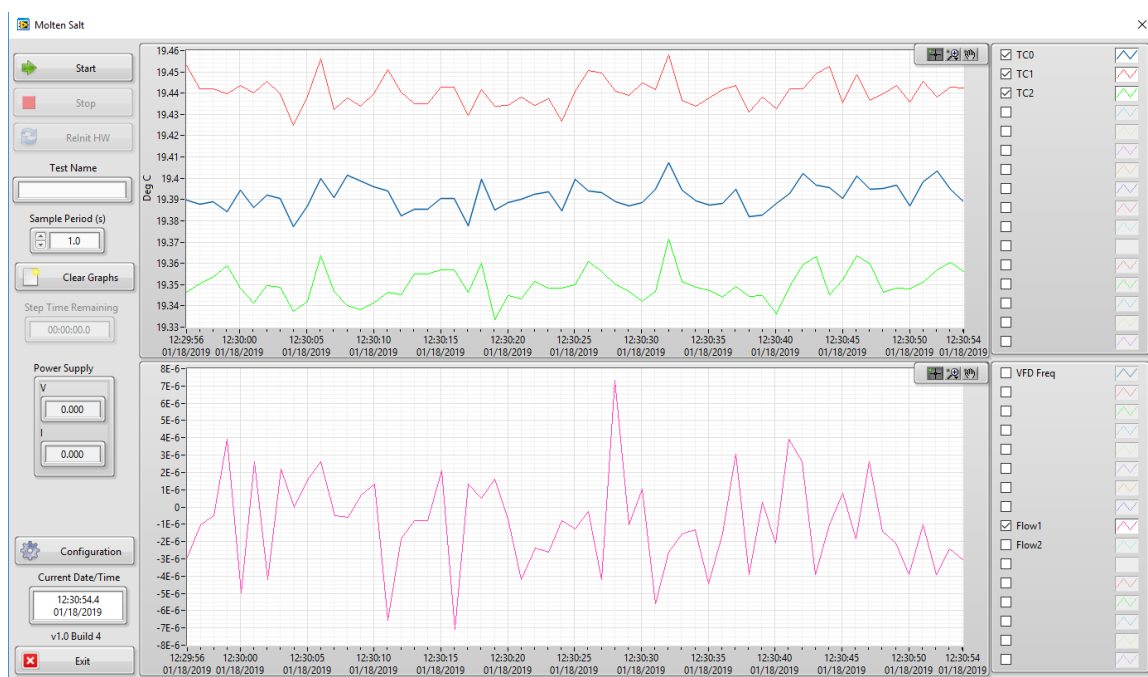
Figure 3-19 LabVIEW software

The next major construction item was assembling the glovebox after its delivery. A Vigor

Tech technician came to UNM and assembled the glovebox over the course of three days.

At this time the loop was moved into the glovebox and system integration began. Figure

3-20 shows the assembled glovebox. The full integration of the loop with the glovebox

was delayed by a missing feedthrough for the thermocouple lines.

Figure 3-20 Fully Assembled Glovebox

After the glovebox assembly and testing, it was opened up for shakedown testing of the

loop. The shakedown tests started with the water and pump calibration test and was

followed by the high temperature molten salt test. Between these tests the flow meter was

removed, and insolation was installed. Figure 3-21 shows the loop in its salt shakedown

configuration with insolation installed. Figure 3-21 shows the assembled loop

configuration at the time of writing.

Figure 3-21 Test loop in salt shakedown configuration

4. Loop Shakedown Testing

A. Water Shakedown Test

The first test of the loop was to operate it with water as the circulating fluid. The goal of the test was to verify that all of the loop components functioned and to measure the correlation between VFD controller frequency and pumping power. When the test

began the pump worked as designed, pumping water through the loop. The data log was started and the flow rate was measured as the pump control frequency was increased from 20 to 60 Hz in 10 Hz increments. At this point it was confirmed that the system runs properly with the designed 1.2 L fluid inventory. Unfortunately, the flow meter didn't function as intended rendering the flowrate data unusable. Because fixing the flow meter wasn't possible at the time and alternate pump calibration method was devise.

For the new pump calibration testing the loop was removed from the pump and tubing was ran from the pump outlet to an empty container. To measure the mass flow rate, a timer was running while water was pumped into the container. With the pumping time and the change in container mass the mass flow rate could be calculated. In turn the pumping power can be calculated from that mass flow rate. The pumping power equation (3-5) introduced earlier in the chapter was used for this purpose.

$$W = \dot{m}g(h + (h_L + h_{Lfitting})) \tag{3-5}$$

In order perform the calculation the head values in the above equation had to be found. There was no elevation head so the first h in the equation could be dropped. The testing set up also only consisted of a single length of tubing, so the fitting head could be drop from equation 3-5. The only head value remaining was the friction head calculated form equation 3-3.

$$h_L = (32/Re)(L/D)(v^2/g) \tag{3-3}$$

To solve for the friction head a conversion between mass flow rate and flow velocity was need. Equation 3-6 is this conversion.

$$v = \frac{\dot{m}}{\rho A} \tag{3-6}$$

v is the fluid velocity. ṁ is the mass flow rate. ρ is the density. A is the tube cross sectional area. Equation 3-6 and 3-3 were substituted into equation 3-5 and then simplified to produce equation 3-7 which is a mass flow rate dependent pumping power equation.

$$P = \frac{128L\mu\dot{m}^2}{\rho^2 \pi D^4}$$

(3-7)

Where P is the pumping power in watts. L is the length of the tubing in meters. μ is the viscosity in Pa*s. ṁ is the mass flow rate in kg/s. ρ is the density in kg/m³. And lastly D is the tubing diameter in meters. For the pump calibration test the length of the tube was 71" (1.8 m) and the tubing diameter was ¼" (.00638 m). Table 3-3 lists the calibration test results as well as the calculated mass flow rate and pumping power. The 50 Hz data was lost due a test procedural error.

Table 3-3 Pump Calibration Results

Frequency (Hz)	Time (s)	M (kg)	ṁ (kg/s)	Power (W)
20	48.16	0.65	0.0135	0.00737
30	36.61	0.75	0.0205	0.01698
40	25.62	0.6	0.0234	0.02219
60	39.4	1.4	0.0355	0.05109

The data from table 3-3 is plotted in figure 3-22. From the plotted data a best fit equation was derived. This equation (3-8) is the frequency dependent pumping power for the pump and is valid from 20Hz to 60Hz.

$$P(W) = 0.0011 * freq(Hz) - 0.0162$$

(3-8)

This pumping power equation will be used in conjunction with equation 3-8 as well as the

physical properties of the salt to calculate the flow rate during high temperature

experiments.
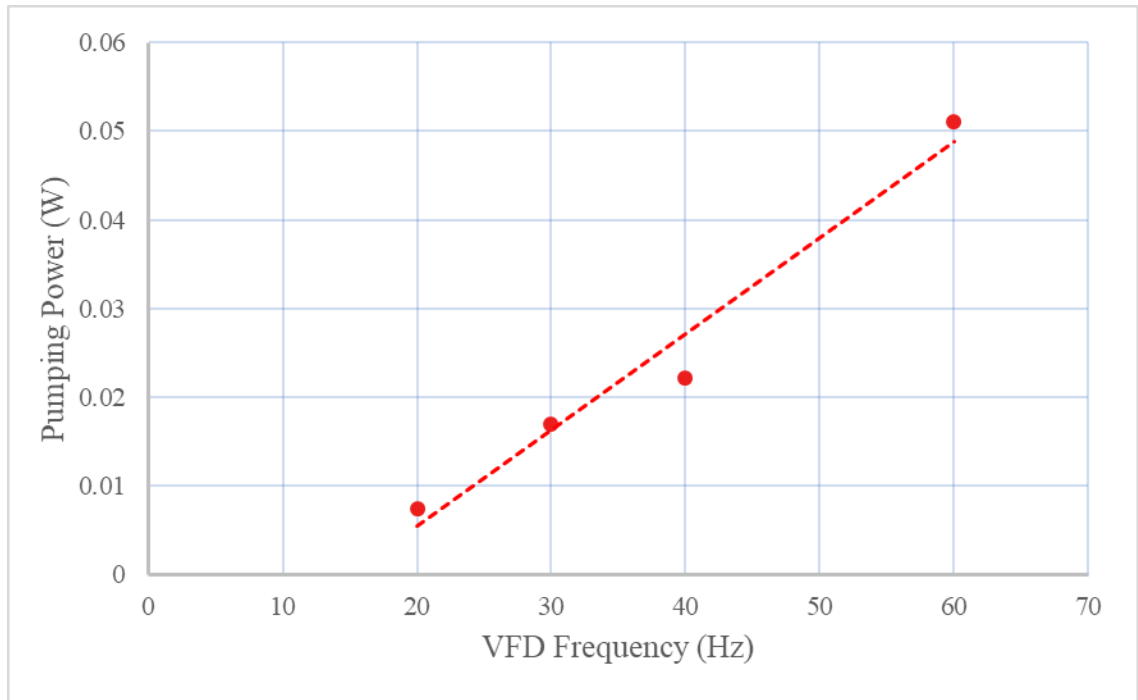
Figure 3-22 Frequency Dependent Pumping Power

B. Molten Salt Shakedown Test

The goal of the molten salt shakedown test was to test the experiment facility at

near FLiBe operating conditions as well as acquire some initial flow accelerated corrosion

data. For the test an alternatively salt was needed which wouldn't require the same safety

procedures as FLiBe. The salt selected was HITEC salt. HITEC salt consists of a mixture

of potassium nitrate, sodium nitrite, and sodium nitrate. HITEC salt is used as a heat

transfer fluid and is know for its application in solar power. The salt melts at 142C and

can operate safely at over 500C making it a suitable material to test the loop facility at

high temperatures. In addition, unlike FLiBe, HITEC salt is generally safe to handle with

minimal safety equipment. Gloves should be worn during handling to avoid skin

irritation, and the salt shouldn't be ingested.

For the test the salt was loaded into the melt tank by hand through the ½" port in

the melt tank lid. Figure 3-23 shows the HITEC salt as delivered. The salt is white in

color and besides a few large clumps consisted of small grains of salt.

Figure 3-23 HITEC salt

Before the test a stainless-steel sample was prepared for corrosion testing. The sample

was cleaned, its dimension taken, and weighed before being loaded into the loop. The

shakedown test would last for 48 hours and any changes in the sample due to corrosion

would be measured.

After loading the sample and the salt, the shakedown test was started. Over the

course of three hours the salt was brought up to 500C melting it. Over the course of the

heating period no issues were observed. Next the pump was turned on and spun up to

operating at full power with a controller frequency of 60 Hz. The loop pumped the high

temperature salt without issue. The temperature of the salt remained constant throughout

the insolated loop section. Based on the observed insolation performance, the heating tape

is not necessary to maintain isothermal conditions around the samples. Therefore, the

heating tape can be omitted from future configurations of the experimental loop. After

observing the facility function perfectly for over an hour, the operator left the lab while

the loop continued to run for its 48-hour shakedown test. Unfortunately, a few hours later

the circuit breaker to the facility tripped terminating the test. Attempts to reset the breaker

demonstrated that it would trip even without running either the pump or melt tank

heaters. This suggests that it is a lab electrical system problem and not a problem with the

flowing FLiBe corrosion test loop. An electrician will be needed to determine the exact

issue.

(a) Test Sample Results

      Before the shakedown test a stainless-steel sample was cleaned, measured, and

weighed. The dimensions of the sample were measured with calipers and the weight

measured on a high accuracy digital scale. Table 3-4 list the before and after

measurements of the sample exposed to 500 ˚C HITEC salt for several hours.

<center>Table 3-4 Salt shakedown sample changes</center>

	Pretest	Post-test
Width	0.530 in	0.530 in
Length	1.450 in	1.450 in
Thickness	0.120 in	0.120 in
Mass	8.11308 g	8.11341 g

The results in table 3-4 show that no measurable change to the sample dimensions

occurred. Figure 3-24 shows a picture of the post test stainless-steel sample next to an

untested sample.

Figure 3-24 Post test sample next to unused sample

The only discernable difference between the exposed and unexposed sample is the

discoloration of the test sample. This discoloration is most likely surface oxidation which

in turn explains the small weight gain the sample experienced. Longer high temperature

testing in flowing molten salt will be needed to determine any corrosion effects.

(b) Post Test System Inspection

After the molten salt shakedown test, the corrosion loop was disassembled and

had its insolation removed for inspection. During disassembly points of salt leakage were

noted by the insolation that adhered to those areas. The first change to the system noted

was the uniform brown discoloration to the stainless-steel. At 500˚C the steel appears to

have lightly oxidized giving it its new light brown hew. Figure 3-25 shows the

discoloration of the metal clearly.

Figure 3-25 Post salt shakedown test loop

The first location noted to have leaked salt was the around the expansion tank.

The salt had leaked through the gasket and solidified after seeping into the surrounding

insolation. Figure 3-26 shows the salt that leaked through the gasket cementing some of

the insolation to the expansion tank. To investigate the leakage the lid was removed from

the expansion tank to inspect the gasket. Figure 3-27 shows the gasket and the interior of

the expansion tank. It was first noted that a layer of salt was deposited on the bottom of

the expansion tank. This could be a potential contamination issue in the future. The

gasket itself seemed unchanged from the test. This indicates that the salt flowed around

the gasket to leak. Base on this observation the thickness of the gasket used in future test

will have to be increase. The current gasket wasn't thick enough to maintain a proper seal

after thermal expansion, so a design correction is needed.

Figure 3-26 Salt leakage around expansion tank gasket

Figure 3-27 Post test expansion tank interior and gasket

The second leak location was around the first 1" Swagelok socket joint after the pump outlet. The leak site is shown in figure 3-28.

Figure 3-28 Pump outlet loop leg salt leak site

Once again, the leakage stopped after hardening in the insolation material. It appears that as a general principle molten salt leaks from the test loop self-seal once a finite amount of salt has hardened in the insolation. The cause of the leak was in adequate tightening of the Swagelok fitting in combination with the pressure of the pump outlet. To prevent future leaks of this type failed joints will be retightened and extra care will be taken when reassembling Swagelok joints.

The last and largest salt leak was from around the melt tank. A significant amount of salt had leaked through melt tank lid gasket and started to flow down the exterior housing. Figure 2-29 shows the leak around the melt tank.
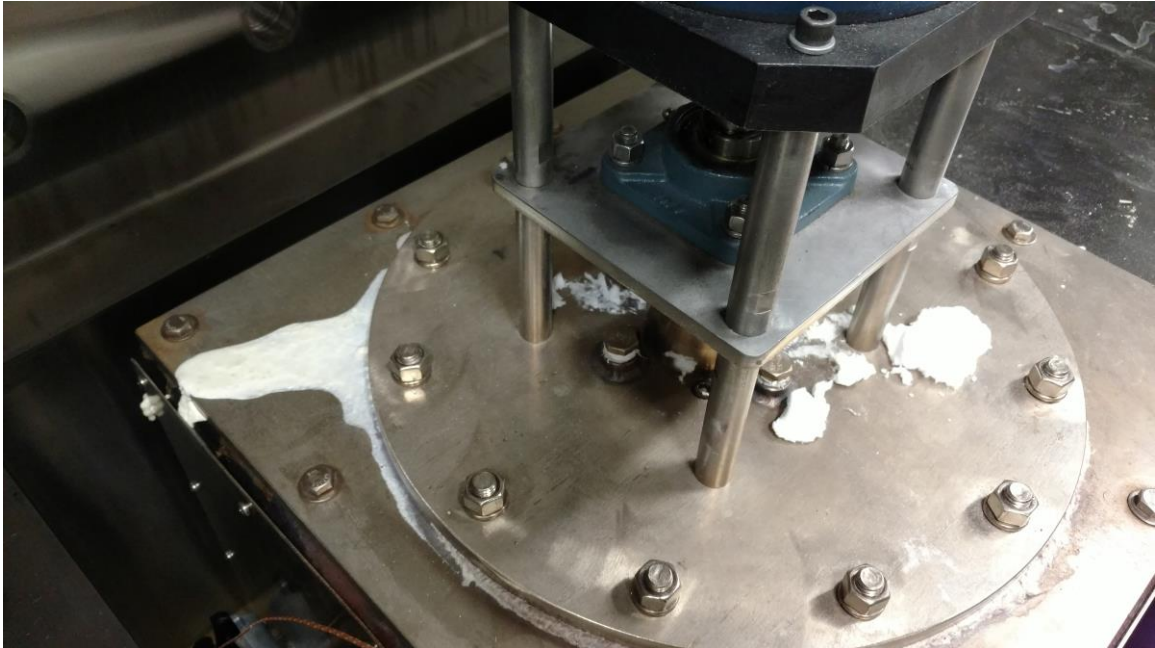
Figure 2-29 Melt tank leak

After inspection it was also noted that the gasket itself was infused with HITEC salt. The cause of this leak was poor loading technique. During loading, salt grains piled up on the pump impeller till the pile reached the melt tank rim at which point some of the salt accumulated on top of the melt tank housing. After melting this free salt began to flow resulting in the leakage seen in figure 2-29. Care will be taken when loading salt in the future to prevent future leaks. One option is to load from the opposite side of the melt tank to avoid salt being deposited on top of the impeller.

All together the test loop performed well during the molten salt shakedown test, and all of the salt leaks have been addressed.

Chapter 4: Flowing FLiBe Corrosion Model

1. Current Models and Their Limits

A key mark of understanding a physical process is the ability to accurately predict the outcome of the process when the starting conditions are known. Such understanding also aids design work by reducing the need for full scale prototyping tests. In the case of flowing FLiBe corrosion, the development of an accurate numerical corrosion model properly validated by experimental results would allow for rapid exploration of the FLiBe design space. The results of such a model would point towards promising solutions to design challenges and support experimental work by providing a more focused testing matrix. For these reasons a multi-physics numerical model of flowing molten fluoride salt corrosion was developed.

Much of the early work with flowing molten salt corrosion took place in conjunction with the Molten Salt Reactor experiment at Oak Ridge National Lab. Much of the supporting corrosion research focused on creating a library of corrosion tests for various materials in a thermal convection test loop.[10] While creating a reference pool of experiments is essential for doing further design work, predicting results not directly tested requires a theoretical framework for extending the results. Since the early loop tests, corrosion models have been created in support of later static FLiBe corrosion tests. These models have typically consisted of a single governing equitation that models a single phenomena. One example is the model used for predicting chromium concentration at increasing depths inside a metal sample exposed to FLiBe. Equation 4-1 works on the assumption that the surface concentration of Cr remains constant at zero and thus Cr loss depends only on internal diffusion.[8]

$$C_{Cr}(x,t) = C_{0,Cr}\,erf\left(\frac{x}{2\sqrt{D_{eff}t}}\right) \qquad (4\text{-}1)$$

Equation 4-1 effectively correlates to its paper's results but is incapable of accounting for any corrosion regime besides metal diffusion limited corrosion.

Another example of a FLiBe corrosion model is the electrochemical model governed by Butler-Vomer equation shown in a paper produced by Virginia Tech.[7] This model calculates the corrosion rate based on the electrochemical reaction that occurs at the metal salt interface. (A more detailed explanation of this method is explained later in the chapter.) While the mentioned paper includes methods for accounting for mass transport and diffusion limited cases the model remains primarily focused on the surface reaction.

A common feature of existing FLiBe corrosion models is the focus on a single physical process. That process could be alloy element diffusion in metal or electrochemical reactions at the metal salt interface, but the generalization of each model is limited to the cases where the modeled process is the limiting case. A general model with wide applicability must take into account multiple physical processes that influence the corrosion.

The newly created FLiBe corrosion model overcomes the limitations of previous models by calculating the solid metal diffusion, surface reaction, and mass transport simultaneously.

2. Model Implementation

A. Overview

Fluoride salt corrosion is distinguished from other typical corrosion conditions by the lack of a passive oxide layer. For corrosion systems, such as in air or water, metal oxides form on the surface of a metal protecting it from further oxidation. In fluoride salt melts such corrosion products dissolve into the melt instead of forming a passive layer.[2] This in turn results in consistent corrosion at the metal salt interface uninhibited by passive oxide layer.

To accurately model fluoride salt corrosion under flow conditions, three separate physical phenomena must be accounted for. The first phenomenon is the diffusion of alloying elements through the metal to the surface. The second phenomenon is the irreversible electrochemical reaction that occurs at interface between that metal and the melt.[7] The last phenomenon is the mass transport of reactants from the melt bulk to the metal surface. Previous models focus for the most part on one of the above phenomena. A general model requires each of the above processes and their interactions to be accounted for.

In the subsequent sections the implementation of each process will be explained. In section B solid metal diffusion is modeled by Fick's second law implemented in an implicit finite difference method. In section C the surface reaction is modeled with Butler-Vomer electrochemical equation. In section D the mass transfer is calculated based on Sherwood number correlations. Section E explains the algorithm for coupling each of the physical phenomena. Section F verifies the performance of the model by

demonstrating diffusion, surface reaction, and mass transport limited cases. Section G

contains the validation of the model against experimental results.

B. Alloy Element Diffusion in the Solid Alloy

According to Fick's hypothesis diffusion is a mass transfer process proportional to

the concentration gradient. This hypothesis is summarized by Fick's first law (eq. 4-2)

$$F = -D \, \delta C / \delta x \tag{4-2}$$

F is the rate of mass transfer over area. D is the diffusion coefficient. C is the

concentration. Lastly x is length.

The diffusion equation is further derived in three dimensions by considering the

case of a rectangular parallelepiped whose sides are aligned with the major axes and the

length of the sides are 2dx, 2dy, and 2dz. The concentration of the diffusing substance is

C. The rate of which the substance enters one of the x perpendicular faces is:

$$4 dy dz \left(F_x - \frac{\delta F_x}{\delta x} dx \right)$$

F_x is the rate of transfer through the side. The equation for the other x perpendicular face

is:

$$4 dy dz \left(F_x + \frac{\delta F_x}{\delta x} dx \right)$$

When combined the net flux in the x direction is:

$$-8 dx dy dz \frac{\delta F_x}{\delta x}$$

The equations in the y and z directions are of the same form. The rate the substance

increases in the volume with time is:

$$8 dx dy dz \frac{\delta C}{\delta t}$$

By combining each term, the concentration in the volume is defined by:

$$\frac{\delta C}{\delta t} + \frac{\delta F_x}{\delta x} + \frac{\delta F_y}{\delta y} + \frac{\delta F_z}{\delta z} = 0$$

By substituting Fick's first law for each of the above flux terms Fick's second law, the

diffusion equation, is derived.

$$\frac{\delta C}{\delta t} = D\left(\frac{\delta^2 C}{\delta x^2} + \frac{\delta^2 C}{\delta y^2} + \frac{\delta^2 C}{\delta z^2}\right)$$

Or when simplified to be one dimensional.

$$\frac{\delta C}{\delta t} = D\frac{\delta^2 C}{\delta x^2} \tag{4-3}$$

Fick's second law (eq. 4-3) is the equation used when solving for the time dependent

concentration in the model.

Fick's second law can be solved analytically for simple cases, however numerical

methods are required for more complex cases such as multiple material layers. The

numerical method selected is the implicit finite difference method. Said method benefits

from not having a solution stability limit. The method works by discretizing a material

into a series of nodes of a finite size. Fick's second law is then solved for the boundaries

of each node. This allows for the calculation of the concentration across discontinuities as

well through multiple materials. Equation 4-4 is an example of Fick's second law

discretizes for the implicit finite difference method.

$$\frac{C_n^{p+1} - C_n^p}{\Delta t} = D_1\frac{C_{n-1}^{p+1} + C_{n+1}^{p+1} - 2C_n^{p+1}}{(\Delta x)^2} \tag{4-4}$$

C is the concentration in moles. p is the timestep counter while n is the node location. D_1

is the diffusion constant of the material in m^2/s and Δx is the distance between each node.

The mass balance equation is then rearranged to group the C_{n-1}^{p+1}, C_n^{p+1}, and C_{n+1}^{p+1} variables (eq. 4-5)

$$\left(1 + 2D_1 \frac{\Delta t}{(\Delta x)^2}\right) C_n^{p+1} - \left(D_1 \frac{\Delta t}{(\Delta x)^2}\right) C_{n-1}^{p+1} - \left(D_1 \frac{\Delta t}{(\Delta x)^2}\right) C_{n+1}^{p+1} = C_n^p \qquad (4\text{-}5)$$

An important feature of the implicit finite difference method is that the concentrations are solved for the next time step based on the adjacent concentrations also at the next time step unlike the forward finite difference method. The implicit finite difference method generates as system of equations based on equation 4-5. The system of equations takes the form of AX = B with A being the coefficient matrix, X being the p+1 concentrations and B being the time step p concentrations. The equation is then solved via matrix mathematics for X. The equations at the boundaries and any material interfaces much be adjusted to take into account the relevant conditions. Table 4-1 lists the node equations used in the implemented model which consists of two materials layered together. The boundaries are presumed to be impermeable.

Table 4-1 Finite Difference Method Node Equations

Region 1 Boundary	$\left(1 + D_1\frac{\Delta t}{(\Delta x)^2}\right)C_n^{p+1} - \left(D_1\frac{\Delta t}{(\Delta x)^2}\right)C_{n+1}^{p+1} = C_n^p$
Region 1 Interior	$\left(1 + 2D_1\frac{\Delta t}{(\Delta x)^2}\right)C_n^{p+1} - \left(D_1\frac{\Delta t}{(\Delta x)^2}\right)C_{n-1}^{p+1} - \left(D_1\frac{\Delta t}{(\Delta x)^2}\right)C_{n+1}^{p+1} = C_n^p$
Material Interface	$\left(1 + D_1\frac{\Delta t}{(\Delta x)^2} + D_2\frac{\Delta t}{(\Delta x)^2}\right)C_n^{p+1} - \left(D_1\frac{\Delta t}{(\Delta x)^2}\right)C_{n-1}^{p+1} - \left(D_2\frac{\Delta t}{(\Delta x)^2}\right)C_{n+1}^{p+1} = C_n^p$
Region 2 Interior	$\left(1 + 2D_2\frac{\Delta t}{(\Delta x)^2}\right)C_n^{p+1} - \left(D_2\frac{\Delta t}{(\Delta x)^2}\right)C_{n-1}^{p+1} - \left(D_2\frac{\Delta t}{(\Delta x)^2}\right)C_{n+1}^{p+1} = C_n^p$
Region 2 Boundary	$\left(1 + D_2\frac{\Delta t}{(\Delta x)^2}\right)C_n^{p+1} - \left(D_2\frac{\Delta t}{(\Delta x)^2}\right)C_{n-1}^{p+1} = C_n^p$

In order to properly validate the diffusion model a simple one material case matching existing experimental work was created. The boundary conditions were set as constant C = 0 for the FLiBe facing surface and dC/dt = 0 for the far surface. These boundary conditions presume that all Cr reacts as soon as it comes into contact with the FLiBe and that no Cr leaves through the other surface. The reference results comes from research conducted at University Wisconsin Madison were stainless steel was exposed to static FLiBe.[2] Included in the results is equation 4-1, mentioned above, that describes the time dependent Cr distribution in the stainless steel. The results from the finite difference method and eq. 4-1 are compared in figure 4-1.
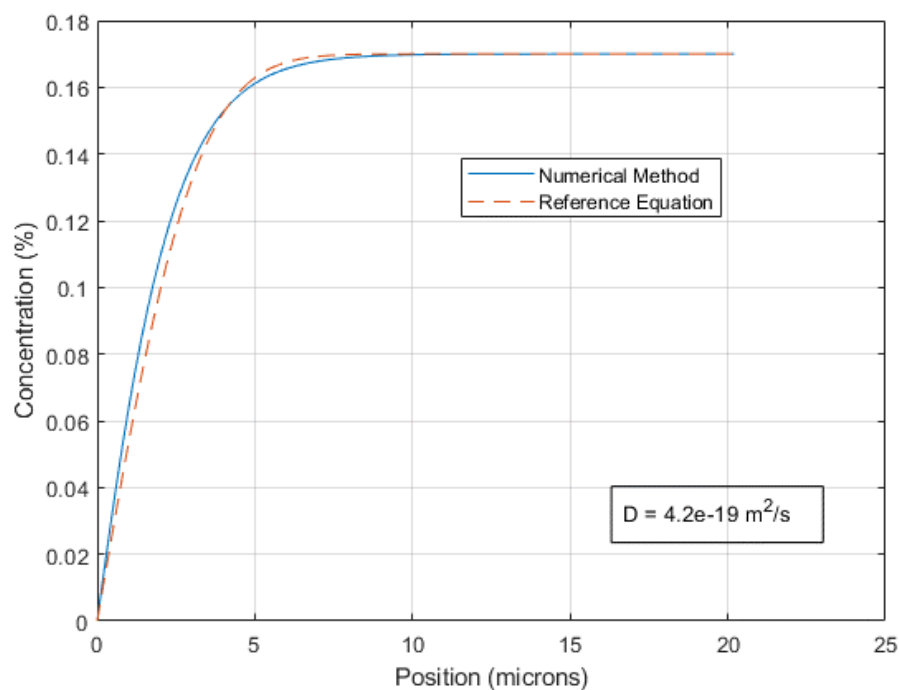
Figure 4-1 Finite Difference Method Validation

Figure 4-1 shows that the implicit finite difference method agrees with existing results for

FLiBe corrosion and can be further used to model Cr diffusion.

C. Surface Reaction Model

Metal corrosion in fluoride salts is an irreversible electrochemical reaction that

occurs at the interface of the salt melt and metal.[7] The metal serves as the anode of the

reaction and dissolves into the melt. Oxidants in the salt serve as the cathode and is

reduced. Whether the reaction occurs spontaneously depends on the Gibbs free energy of

formation. Equation 4-6 show the electrochemical Gibbs free energy equation.

$$\Delta G = -nF\Delta E \tag{4-6}$$

ΔG is the Gibbs free energy and has units of J/mol. F is the Faraday constant, 96,485

C/mol. n is the number of charges exchanged in the reaction. Lastly ΔE is the potential

difference between the cathode and the anode. If the anode has a smaller potential than

the cathode then the reaction occurs spontaneously. In the case of steels the expected

reaction is the reduction of NiF_2 (reference potential -2.42 V[7]) and the oxidation of Cr

(reference potential -3.28 V[7]). NiF_2 is an impurity of concern in the molten salt while Cr

is a common alloying element in structural metals. The expected result of the

electrochemical process is the deposition of Ni and the dissolution of Cr into the salt.

The electrochemical reduction process for each element is governed by the Butler-

Volmer equation (equation 4-7).

$$i = i_o \left\{ exp\left[\frac{(1-\alpha)nF}{RT} \eta \right] - exp\left[\frac{-\alpha nF}{RT} \eta \right] \right\} \tag{4-7}$$

Where i is the current density (A/cm^2), i_o is the exchange current density (A/cm^2), α is the

charge transfer coefficient, n is the charge of the ion, F is the Faraday constant, R is the

gas constant, T is the temperature, and η is the overpotential which equals $E_{electrode} -$

$E_{equilibrium}$. The electrode potential is the potential actually experienced while the

equilibrium potential is the potential when the reactants are at equilibrium concentrations.

Equation 4-8 is used to calculate the equilibrium potential.

$$E_{M^{n+}/M} = E^*_{M^{n+}/M} + \frac{RT}{nF} \ln \frac{C_{M^{n+}}}{C_M} \tag{4-8}$$

E^* is the tabulated formal potential. R is the gas constant. T is the temperature. And C is

the concentration of metal fluoride in the melt and the solid metal in the alloy. Equation

4-9 is the equation for the exchange current density.

$$i_o = nFk°C_{M(n)}^{b}{}^{1-\alpha} X_M{}^\alpha \tag{4-9}$$

Where $k°$ is the reaction rate, C is the bulk concentration in the fluid, and X is the

concentration in the metal. The corrosion rate is determined by calculating the current

density curves for each reactant and finding the electrode potential at which the sum of

the current densities is zero, or in other words when the oxidation rate matches the

reduction rate. Current density is related to species flux by equation 4-10.

$$i = nFJ \qquad (4\text{-}10)$$

Where J is flux in units of mol/cm²s. The surface flux in this case is the corrosion, and the

mass loss can be derived from the atomic weight of the corroding metal atoms.

D. Flowing Fluid Mass Transport

In the course of the electrochemical surface reaction, the oxidant salt in the melt is

reduced at the corrosion surface and is depleted. Oxidant salt depleted this way is

replaced by the mass transport of the oxidant from the fluid bulk to the surface. In the

case that the oxidant is depleted faster that it can be replenished via transport, the reaction

becomes mass transport limited. Equation 4-11 is the current density equation for the

oxidant via mass transport.[7]

$$i_c = nFk_m \left(c_{Ox}^b - c_{Ox}^s \right) \qquad (4\text{-}11)$$

Where k_m is the mass transfer coefficient and c^b and c^s are the bulk and surface

concentration of the oxidant respectively. The maximum mass transport current density

occurs when the melt at the metal surface is completely depleted and surface

concentration becomes effectively zero. Equation 4-12 shows this limiting case.

$$i_L^{ox} = nFk_m C_{ox}^b \qquad (4\text{-}12)$$

The transport limited current density shown in equation 4-12 effectively represents the

maximum possible corrosion rate for the system. The corrosion rate can only exceed this

value for the period of time it takes to deplete the surface concentration of oxidant, after

which the corrosion rate promptly drops to the limiting value.

Calculating the mass transport limited current density requires that the mass transfer coefficient for the system be first calculated. This value can be derived from the Sherwood number for the system which when solved for the mass transport takes the form of equation 4-13.

$$k_m = \frac{D}{L} A Re^{\alpha} Sc^{\beta} \tag{4-13}$$

Where D is the diffusivity of the oxidant, L is the characteristic length, Re is the Reynold's number, and Sc is the Schmidt number. A, α, and β are constants dependent on the correlation empirically determined for the system. For these values the Dittus-Boelter equation[11] can be used with the heat-mass transfer analogy. Equation 4-14 shows equation 4-13 with the Dittus-Boelter equations included.

$$k_m = \frac{D}{L} 0.023 Re^{0.8} Sc^{0.4} \tag{4-14}$$

The equations for the Reynold's and Schmidt numbers are shown in equations 4-15 and 4-16 respectively.

$$Re = \rho v L / \mu \tag{4-15}$$

$$Sc = \mu / \rho D \tag{4-16}$$

Where ρ is the density of the fluid, v is the fluid velocity, and μ is the dynamic viscosity. All together this allows for the calculation of the mass transfer coefficient and in turn the limiting current density.

E. Model Coupling and Implementation

Having established models for the solid metal diffusion, the surface reaction, and the mass transfer limit of the surface reaction, these three models must be combined to

create a comprehensive model. This section lays out the step by step process of coupling

the models together and lists the constants used and their sources.

The model is an iterative algorithim. This means that the entire model is solved

for one timestep before proceeding to the next. Step one is solving the implicit finite

difference method matrix for the metal concentrations for the time step. Step two is

solving for the exchange current density (equation 4-9) using the surface concentration of

chromium calculated in step one. This step couples the solid diffusion model to the

surface reaction. For step three the Butler-Volmer equation (equation 4-7) is solved for

chromium and nickel (or iron depending on melt impurities) using the exchange current

density calculated in step two. Chromium in the case of typical FLiBe corrosion is the

dissolving anode and nickel (or iron) fluoride is the depositing cathode. To find the

correct electrode potential the solution space of the Butler-Volmer equation is searched.

The first search consists of calculating the results of the Butler-Volmer equation over a

range of expected electrode potentials. Then the electrode potential which produces the

smallest difference between the nickel and chromium current density is selected. A finer

search is then conducted around the previous best electrode potential. This process is

repeated four times. After this process is done step three has produced the current density

for the surface reaction. Step four compares the current density from step three to the

mass transport limited maximum current density calculated based on the flow conditions.

If the current density exceeds the limiting value, the corrosion rate is downgraded to the

mass transport limited value. Step four is the point at which the fluid flow effects are

coupled to the model. Step five consists of converting the reaction current density to a

flux with equation 4-10. Based on the derived flux the mass loss for the time step is

calculated and subtracted from the surface concentration of the metal. At this point the

process starts over again at step one. This entire solution is summarized in table 4-2.

Table 4-2 Model Coupling Algorithm

Step 1	Solve implicit finite difference method for Cr concentration in the metal
Step 2	Solve for exchange current density based on surface concentration from step 1
Step 3	Search for best electrode potential and solve for reaction current density
Step 4	Compare/correct step 3 current density with mass transfer limit current density
Step 5	Convert current density to a flux and update the metal surface concentration

The above algorithm calculates the corrosion rate for metal alloys in flowing FLiBe. It

couples the alloy element diffusion in metal and flow effects with the surface

electrochemical reaction to comprehensively model the corrosion. This section finishes

with table 4-3 which lists the constants used in the above algorithm. Unless otherwise

noted the values in table 4-3 are used for all of the subsequent model results.

Table 4-3 List of Constants

D Cr in Nickel	$9.5e-17$ m^2/s[12]	α Cr	0.32[16]
D Cr in Nickel	$2.55e-19$ m^2/s[13]	α Fe	0.09[16]
D Cr in Incoloy 800H	$9.415e-16$ m^2/s[14]	α Ni	0.50[7]
D Cr in Incoloy 800H	$2.0e-17$ m^2/s[15]	ρ FLiBe @ 700 ℃	1671.1 kg/m^3[7]
D Cr in Incoloy 800H	$6.0e-18$ m^2/s[15]	μ FLiBe @ 700 ℃	$5.50e-3$ Pa*s[7]
D NiF$_2$ in FLiBe	$5.0e-10$ m^2/s[7]	E reference Cr	-3.28 V[7]
k$_0$ Cr	$2.17e-10$ /s*cm^2[16]	E reference Fe	-2.92 V[7]
K$_0$ Fe	$5.77e-9$ /s*cm^2[16]	E reference Ni	-2.42 V[7]
k$_0$ Ni	$5.77e-11$ /s*cm^2[16,7]		

F. Code Verification

After implementing the model, it is necessary to verify that it is performing as expected. The key features of the model are the alloy element diffusion, surface reaction, and the flow effect model. In order to verify that the model is acting as expected the diffusion limited, reaction rate limited, and mass transport limited cases must be demonstrated to show that each component of the model is capable of impacting the results. The limiting cases were chosen because differences at the extremes are simplest to observe. The following three subsections illustrate each of the limiting cases in turn.

a. Solid Diffusion Limited Case

In the case that the corrosion rate is limited by the solid alloy element diffusion a number of phenomena are expected. First, when the diffusivity of the metal decreases the mass loss rate due to corrosion for the system decreases. Second, the surface concentration of chromium in the metal will drop to zero because the surface reaction consumes the Cr faster than it diffuses to the surface.

To verify the model three simulations were run. The first simulation modeled flowing FLiBe corrosion at typical values and the metal diffusion coefficient was set at 9.415e-16 m^2/s (the most diffusion value for Incoloy 800H[14]). The subsequent simulations were identical to the first except that the diffusion coefficients were set at 9.415e-18 m^2/s and then 9.415e-20 m^2/s. Figure 4-2 shows the resulting mass loss rates for the simulations.
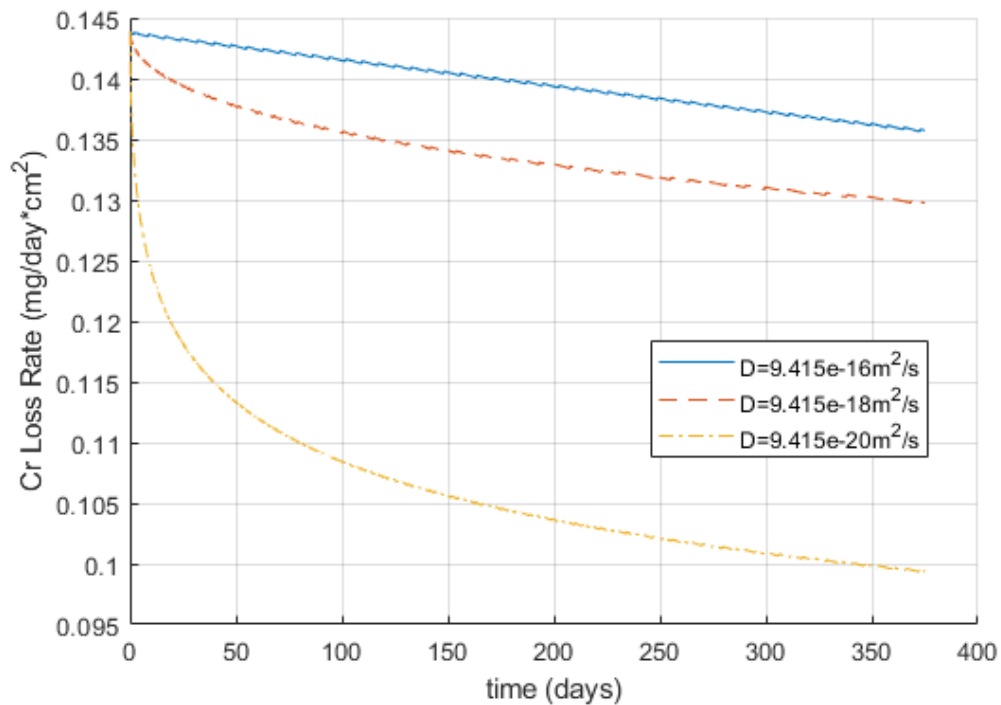

Figure 4-2 Mass Loss Rate for Diffusion Limited Verification Case

As expected, the mass loss rate for the low diffusivity cases drop off as the surface

chromium is depleted in the reaction and replacement chromium diffuses slowly to the

surface. The mass loss rate continues to drop over time for the limited cases due to the

concentration gradient smoothing out over time resulting in less transport to the surface.

As expected, a lower diffusion coefficient results in the loss rate dropping off faster. For

the reference case, the drop in mass loss rate is due to the drop in overall chromium

concentration in the finite system. Figure 4-3 illustrates the change in the concentration of

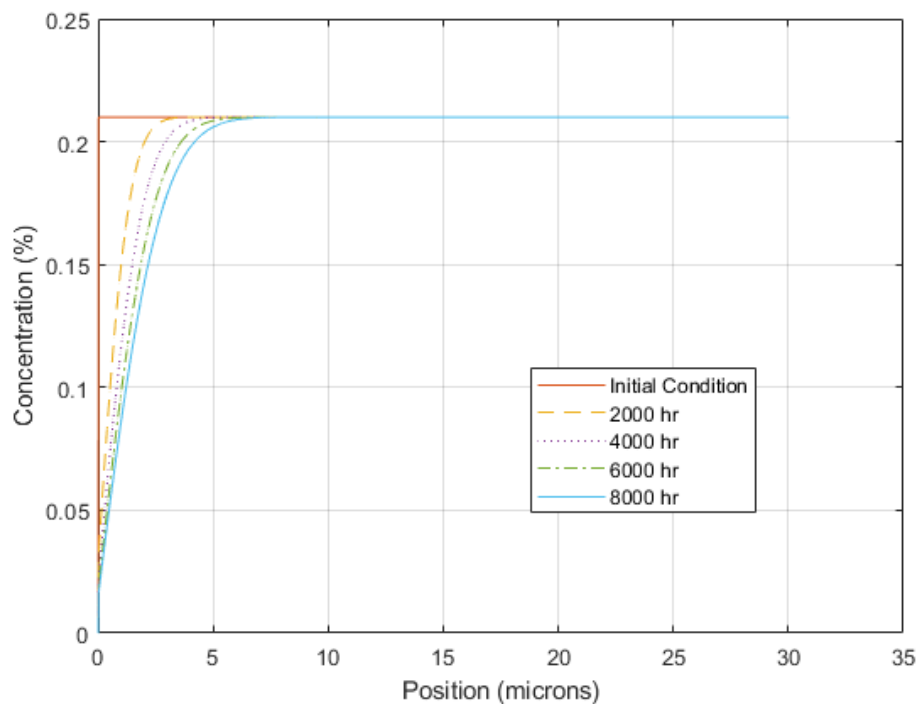chromium in the metal allow over time for the lowest diffusivity case.

Figure 4-3 Cr Concentrations for the Diffusion Limited Case

The shape of the chromium distribution in figure 4-3 demonstrates surface depletion of

Cr. This marks another point of verification that the model behaves as expected when the

diffusion coefficient of the alloy is reduced. All in all, this demonstrates that the model responds properly to changes in the alloy diffusion coefficient.

b. Surface Reaction Rate Limited Case

The reaction rate of the surface reaction directly determines the rate of corrosion in flowing FLiBe. In the case when the reaction rate coefficient is small, the reaction rate limited case arises. When reaction rate coefficients for the electrochemical reactions are reduced the mass loss rate for the model should also decrease. The concentration gradient in the metal should also remain relatively flat because diffusion in the metal smooths out any chromium loss in the alloy. Figure 4-4 illustrates the mass loss rate drop that occurs when the reaction rate coefficients are decreased first to 33% then 10% of their original value.
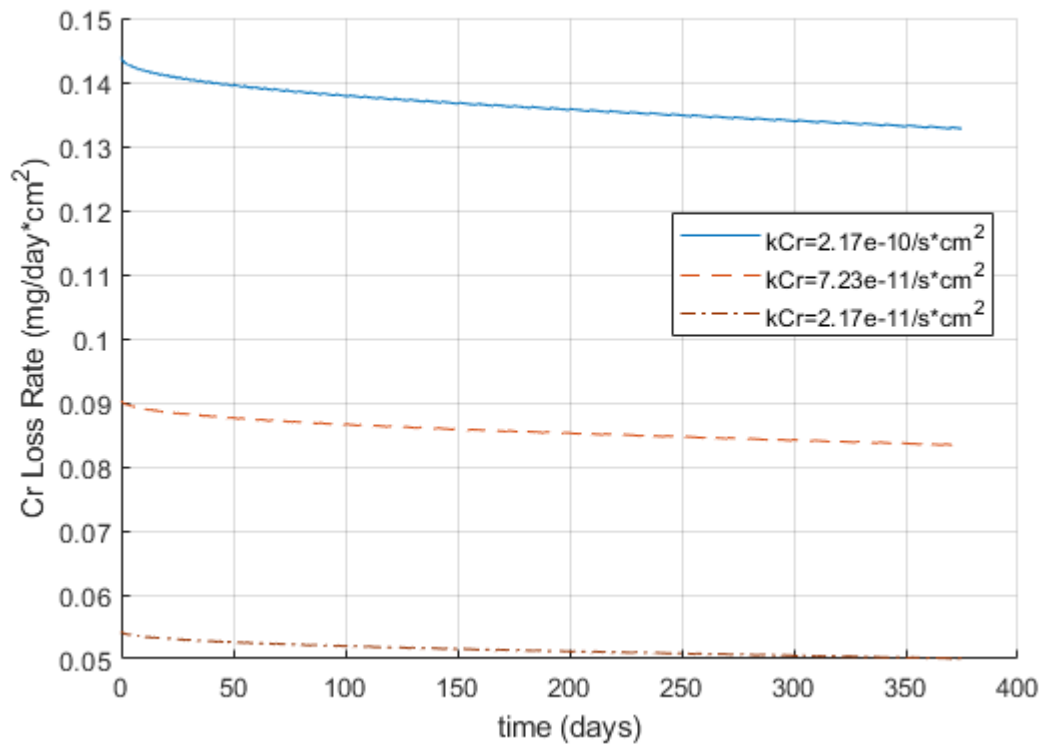

Figure 4-4 Mass Loss Rate for Reaction Rate Limited Verification Case

As one would expect, the mass loss rate drops significantly when the reaction rate coefficients are decreased. The mass loss rate for the limited case decreases slower than the diffusion limited case because the change in surface concentration of chromium drops much slower. This slow drop in surface concentration is illustrated in figure 4-5 which shows the concentration gradient for the surface reaction limited case.
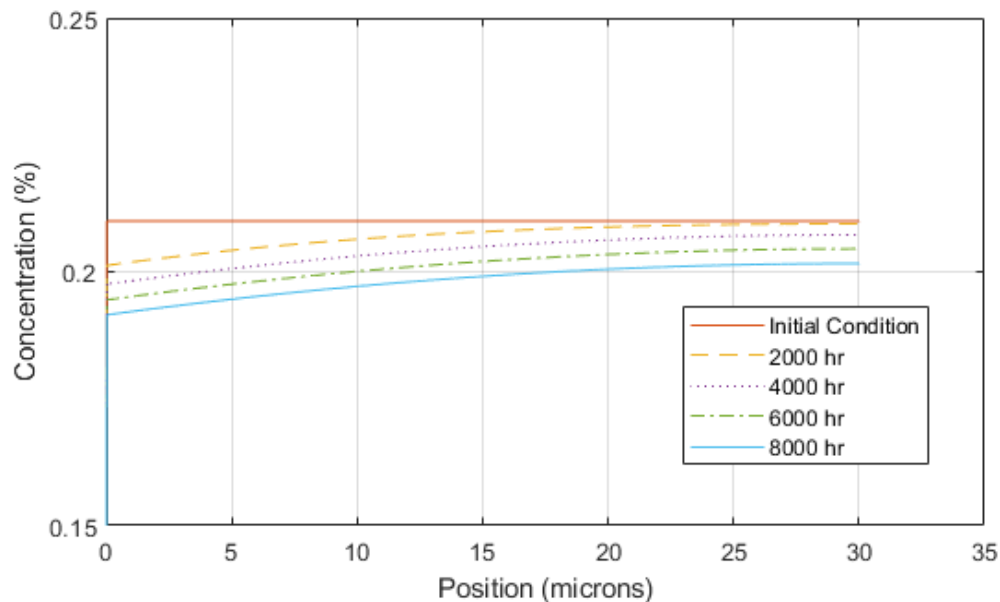

Figure 4-5 Cr Concentrations for the Reaction Rate Limited Case

Altogether, the above results show that the model responds as predicted to changes in the reaction rate at the material surface.

c. Mass Transport Limited Case

In the mass transport limited case oxidants in the melt are consumed at the surface faster than they are transported there. This produces an effective zero surface concentration which in turn causes the maximum rate of mass transport between the fluid bulk and the surface. The surface reaction rate in turn is reduced to the mass transfer rate.

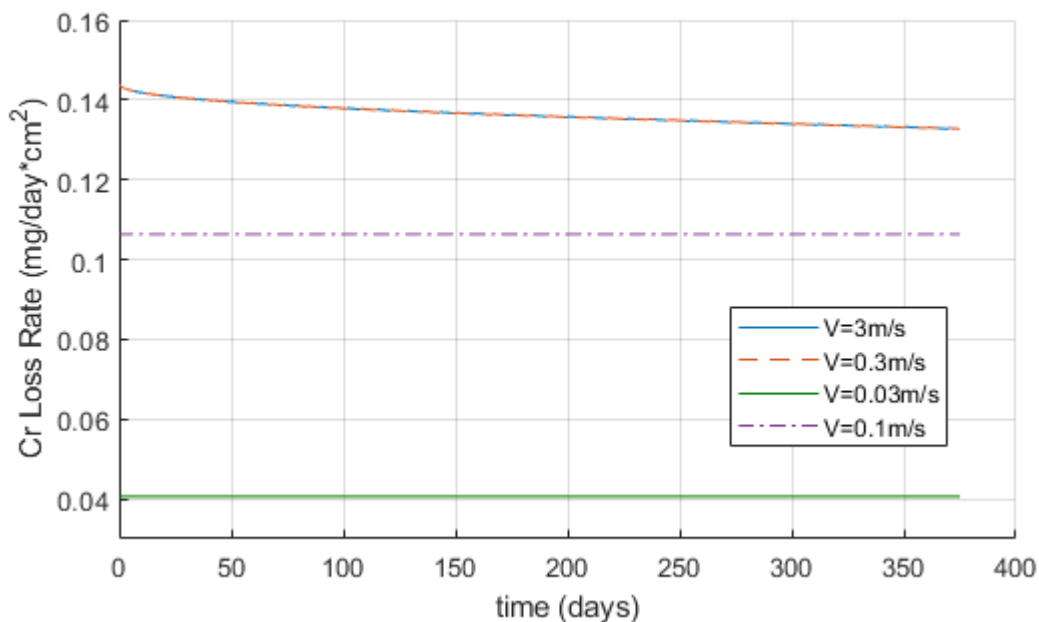Figure 4-6 shows the change in the mass loss rate over time when the flow rate of the FLiBe is reduced.

Figure 4-6 Mass Loss Rate for Transport Limited Verification Case

Figure 4-6 shows the expect result that the mass loss rate in the transport limited case becomes constant. This constant rate matches the maximum mass transport possible under the existing flow conditions. The threshold for the mass transport limited case is the point at which the available oxidants at the surface can no longer consume all the surface Cr. Before this point the system is in the diffusion limited case. It should be noted that even for a two order of magnitude drop in the flow rate the mass loss is only reduced by about 66%. The diffusion coefficients of the oxidants in the melt are large relative to the overall corrosion rate. This means that the corrosion of metal in flowing FLiBe would be expected to show less response to changes in flow conditions. Figure 4-7 is included to show the chromium concentrations over time for the mass transport limited case.
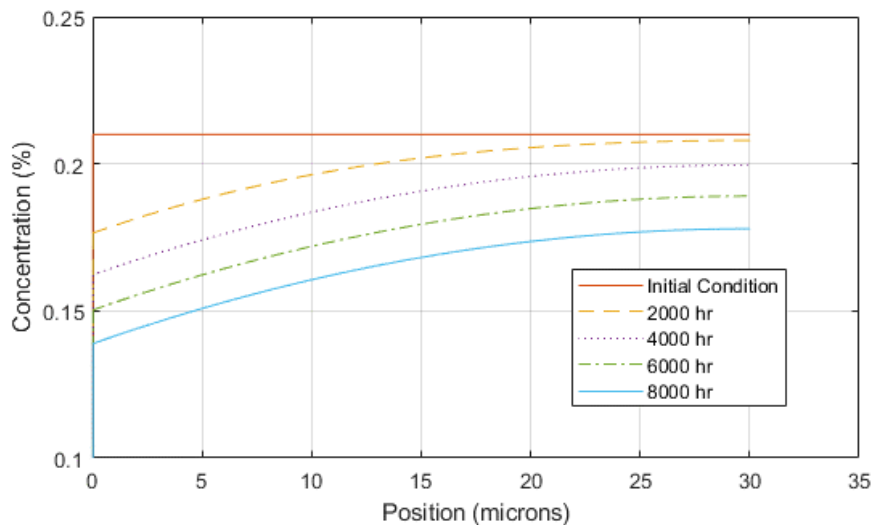
Figure 4-7 Cr Concentrations for Mass Transport Limited Case

The above verification cases demonstrate that the model effectively incorporates the physics of solid alloy diffusion, electrochemical redox reactions, and mass transport under flowing conditions.

G. Model Validation

Having verified that the model responds to changes in corrosion conditions in a physically rational manner, validation of the code against experimental results is required. The Oak Ridge convection loop experiments referred to in the introduction of this chapter was selected for model validation. Table 4-4 summarizes the model inputs drawn from the research paper.[10] All values shown in table 4-4 come from the Oak Ridge paper except for the stainless-steel diffusion coefficient which was taken from published values.

Table 4-4 Validation Case Values

Parameter	Value	Parameter	Value
D 316 SS	4.2e-19 m^2/s[7]	C_{Fe}	1.9e-4
L	0.0254 m	T	650°C
V	0.0167 m/s	Mloss 500 hr	.45 mg/cm^2
C_{Cr}	6.0e-5	Mloss 1000 hr	.65 mg/cm^2

The Oak Ridge experiment was selected as the validation case for several reasons. First,

the experiment exposed metal samples to flowing FLiBe which is exactly the physical

conditions the model was designed to replicate. The overall number of published flowing

fluoride salt corrosion experiments are low, and most of the experiments conducted with

FLiBe flow in tubing were conducted at Oak Ridge. This is part of the reason that there is

currently renewed interest in flowing FLiBe corrosion experiments. Continuing from the

last point, the experiment was conducted in standard tubing. More recent experiments

which include flowing FLiBe corrosion tend to have experimental set ups where the

molten FLiBe is in a flask mixed by an impeller.[4] The mass transport portion of the

model is ill suited to such exotic flow conditions. Lastly, the Oak Ridge paper includes

important values such as the flow speed and geometry as well as the concentrations of

oxidizing contaminants in the salt. All together the Oak Ridge experiment was a natural

choice for the validation case.

Figure 4-8 shows the mass loss results of the model compared to experimental

results. The uncertainty represents the possible unreported contaminates in the salt that

could accelerate corrosion. These uncertain unreported impurities are represented by

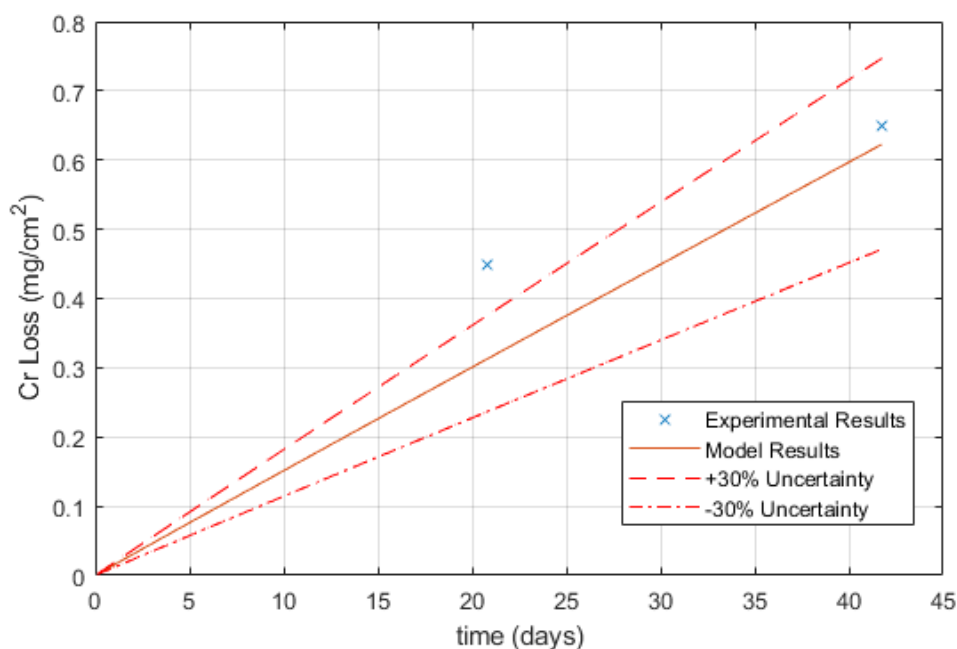adding or taking away from the FeF$_2$ concentration.

Figure 4-8 Model Calculated Mass Loss vs Validation Case Values

Overall the model agrees well with the Oak Ridge experiment. Underestimating the 500

hour mass loss is to be expected because corrosion in FLiBe is initial accelerated by

additional contaminants such as water.[2] These starting oxidants are rapidly consumed.

The long term corrosion rate is determined by metal oxidants like nickel and iron

fluoride. Another possible source of uncertainty is the unspecified diffusivity of the

stainless steel samples. Metal diffusion coefficients can vary greatly with microstructure.

In general diffusion along grain boundaries occurs much faster than in grains, thus metals

with finer grain structures also have larger diffusion coefficients.[7] Despite these

challenges, the above result shows that when the physical parameters can be well

matched, the model accurately predicts mass loss.

3. Model Applications to the FHR System

Having explained the model's implementation and demonstrated its validity, its application to the FHR design is now investigated.

A. Bimetallic vs Single Alloy Materials

One of the areas of investigation for the research connected with this thesis is the application of bimetallic alloys to fluoride salt systems. The bimetallic alloy consists of Incoloy 800H coextruded with a pure nickel surface layer. The nickel is intended as corrosion protection for the underlying structural material. Investigation of such bimetallic alloys was the primary motivator for designing the FDM method in section 2B to use multiple material substrates. Extruding the nickel layer as opposed to electroplating has the additional benefit of creating a nickel microstructure that is more resistant to chromium diffusion. Electroplating produces a very fine microstructure which in turn result in a high diffusivity coefficient.[12] These features together promise to produce a structural material for FHR reactors that is highly resistant to FLiBe corrosion.

In order to investigate the potential benefits of using a bimetallic alloy in an FHR design, the mass loss rate of bimetallic alloys of various nickel thickness were modeled. Values from table 4-3 were used for the investigation with 2.55e-19 m^2/s and 2.0e-17 m^2/s used as the diffusion coefficients for nickel and Incoloy 800H respectively. Figure 4-9 shows the resulting mass loss rates of bimetallic alloys 5, 10, and 15 micrometers thick as well as the mass loss rate of bare Incoloy 800H for comparison.
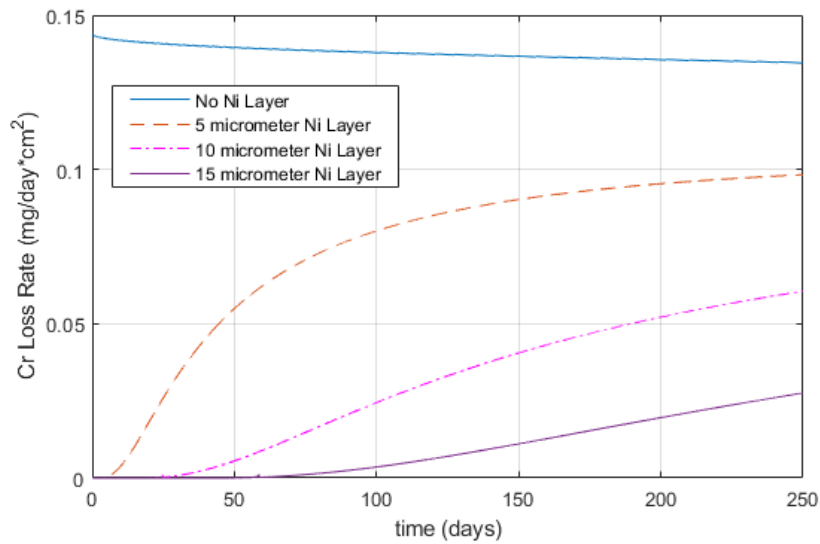
Figure 4-9 Mass Loss Rate for Bimetallic Alloy of Varying Ni Thickness

The results show that increasing the thickness of nickel surface layer not only reduces the

mass loss rate for the metal but also delays the onset of corrosion. The nickel surface

layer acts as a barrier to chromium loss. Chromium must first diffuse through the nickel

substrate to the metal surface before it can react electrochemically with the FLiBe. Figure

4-10 shows the development of the Cr concentration profile of bimetallic alloy.
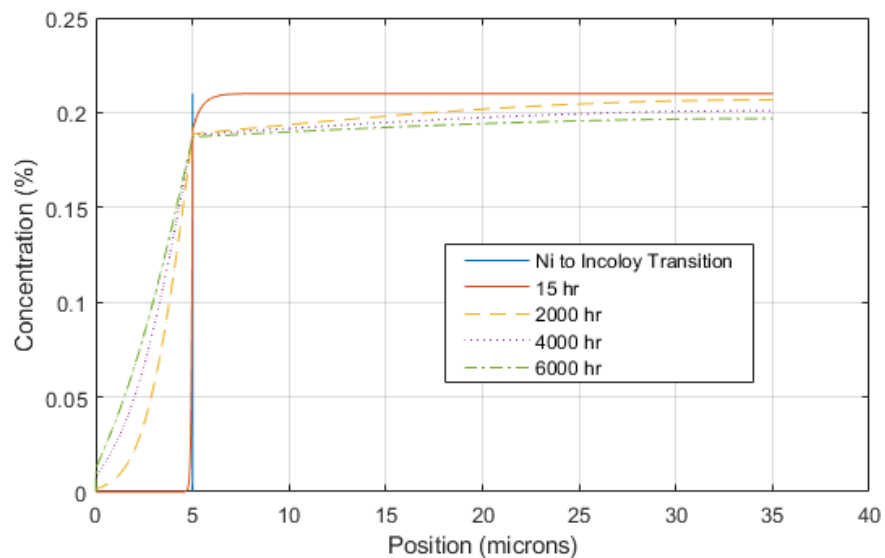

Figure 4-10 Cr Concentration in Bimetallic Alloy (5 μm Ni)

Initially in the bimetallic alloy there is no surface chromium as shown with the 15 hour line in figure 4-10. Over time chromium diffuses into the nickel layer flattening the concentration gradient throughout the layer as shown in the 2000, 4000, and 6000 hour plots. The concentration gradient stabilizes as a linear gradient between the metal surface chromium concentration and the Incoloy 800H Cr concentration develops. The peak mass loss rate in the bimetallic alloy occurs once this equilibrium concentration gradient is reached.

All together the above results show the performance advantages a bimetallic alloy has in corrosion performance. The nickel layer places a cap on the mass loss rate significantly below that of a bare metal. In the next section a bimetallic alloy is applied to the mark-1 pebble-bed fluoride high temperature reactor (PB-FHR) to demonstrate the engineering benefits of bimetallic alloys when applied to an actual design.

B. Bimetallic Alloy Performance Impact on FHR Heat Exchanger Tubes

The Mark-1 PB-FHR pre-conceptual design was produced by UC Berkeley in collaboration with MIT and the University of Wisconsin, Madison.[1] The design is for a small modular fluoride salt cooled reactor and includes parameters for the entire reactor system including the core and heat exchanger system. For this design study the one year mass loss from the heat exchanger tubes were investigated. The material of the heat exchanger tubes in the design is stainless steel.[11] The benefits of applying a bimetallic nickel layer to existing stainless steel was modeled. Table 4-5 lists the values taken from the mark-1 design; other values were taken from the sources previously listed.

Table 4-5 FHR Heat Exchanger Parameters

Parameter	Value
OD Tube	6.350 mm
Tube Thickness	0.889 mm
V Flow	1.09 m/s

Oxidant concentrations were taken from the minimum FLiBe purity standards used for the MSR at Oak Ridge which were 25 parts per million Cr and Ni.[2] The mass loss for bare 316 SS, a 5 μm Ni layer, and a 10 μm layer were modeled.

Figures 4-11 and 4-12 show the mass loss rate and total mass lost for FHR heat exchanger tubing.
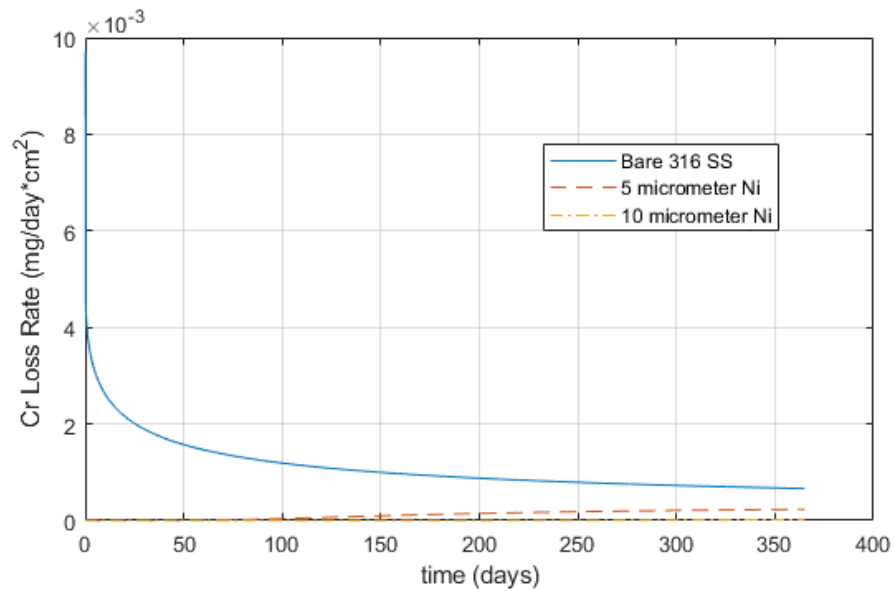

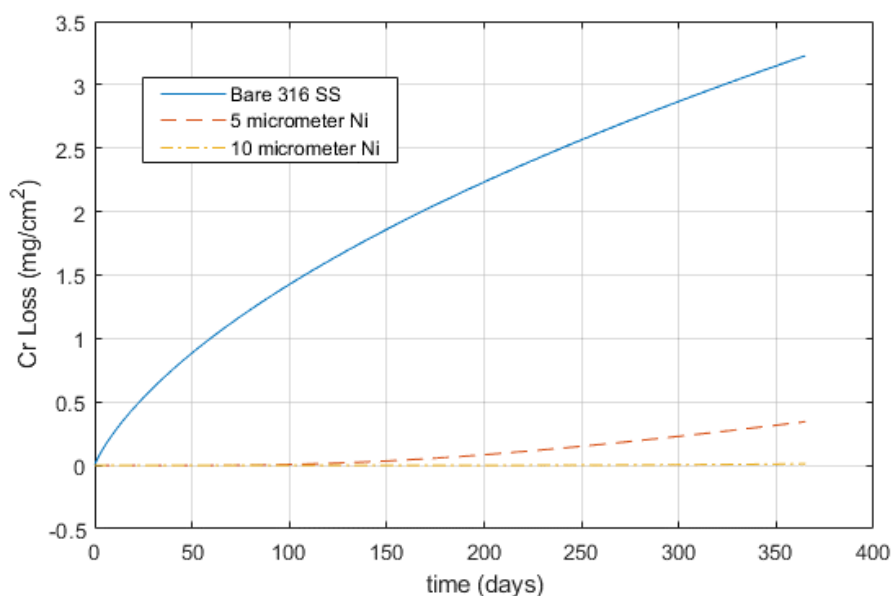Figure 4-11 Mass Loss Rate FHR Heat Exchanger Tubing

Figure 4-12 Mass Loss for FHR Heat Exchanger Tubing

The one year mass loss was 3.23, 0.34, and 0.013 mg/cm^2 for bare 316 SS, 5 μm Ni, and 10 μm Ni respectively. The performance gains from adding a nickel surface laying in the heat exchanger tubing is substantial. Five micrometers of nickel decrease the mass loss in the heat exchanger tubing by an order of magnitude. Ten micrometers decreases the mass loss by two orders of magnitude. Bimetallic alloys have the potential to extend the service life of an FHR heat exchanger bundle a hundred-fold. Due to limitations in the manufacturing process, the nickel layer in actual bimetallic tubing is likely to be much thicker than modeled above. This suggests that actual bimetallic tubing would have even better performance. With such performance compared to traditional tubing, bimetallic tubing will likely be lifetime cost competitive against single metal tubing despite its higher manufacturing cost.

All together the modeling work suggests that bimetallic alloys can dramatically improve the corrosion performance of molten FLiBe systems. Such results give new impetus for investigating composite materials for use in molten FLiBe systems.

4. Conclusion

The multiphysics FLiBe corrosion model developed in this chapter successfully models the solid alloy diffusion, surface electrochemical reaction, and the flow mass transport effects that occur during flowing FLiBe corrosion. The model was verified to perform as expected and validated against a flowing FLiBe corrosion experiment conducted at Oak Ridge Nation Laboratory. Further, the model was used to show the impressive corrosion resistance bimetallic alloys have in flowing FLiBe. All together this demonstrates the benefits of the developed corrosion model as an engineering tool. This model will be further validated against the experimental result of the flowing FLiBe corrosion test loop described in the previous chapters. Altogether, the model described in this chapter is a valuable tool for designing corrosion resistant materials for molten FLiBe systems.

References

1.   C. Andreades, et al, "Technical Description of the "Mark 1" Pebble-Bed Fluoride-Salt-Cooled High-Temperature Reactor (PB-FHR) Power Plant," University of California Berkeley, UCBTH-14-002, 2014.

2.   M. Anderson et al, "Heat Transfer Salts for Nuclear Reactor Systems – Chemistry Control, Corrosion Mitigation, and Modeling," CFP-10-100, University of Wisconsin, Madison (2016).

3.   H. G. MacPherson, "The Molten Salt Reactor Adventure," *Nuclear Science and Engineering*, **90**, 374-380 (1985).

4.   M. Kondo, et al, "Flow accelerated corrosion and erosion-corrosion of RAFM steel in liquid breeders," *Fusion Engineering and Design*, **86**, 2500-2503 (2011).

5.   E. M. Baum et al, *Nuclides and Isotopes: Chart of the Nuclides*, 17th edition, Knolls Atomic Power Laboratory, (2010).

6.   R. Serrano-Lopez, J. Fradera, S. Cuesta-Lopez, "Molten salts database for energy applications," *Chemical Engineering and Processing: Process Intensification*, **73**, 87-102 (2013).

7.   S. Guo, J. Zhang, W. Wu, W. Zhou, "Corrosion in the molten fluoride and chloride salts and materials development for nuclear applications," *Progress in Materials Science,* **97**, 448-487 (2018).

8.   G. Zheng, L. He, D. Carpenter, K. Sridharan, "Corrosion-induced microstructural developments in 316 stainless steel during exposure to molten Li_2BeF_4(FLiBe) salt," *Journal of Nuclear Materials,* **482**, 147 (2016).

9.   M. Straka, M. Korenko, F. Lisy, "Electrochemistry of uranium in LiF-BeF$_2$ melt," *Journal of Radioanalytical and Nuclear Chemistry,* **284**, 245-252 (2010).

10.   J. Keiser, J. DeVan, D. Manning, "The Corrosion Resistance of Type 316 Stainless Steel to Li$_2$BeF$_4$," ORNL/TM-5782 (1977).

11.   M. El-Wakil, *Nuclear Heat Transport,* La Grange Park: American Nuclear Society, 1978.

12.   L. Olson, K. Sridharan, M. Anderson, T. Allen, "Nickel-plating for active metal dissolution resistance in molten fluoride salts," *Journal of Nuclear Materials,* **411**, 51-19 (2011).

13.   C. Smithells, et al, *Smithells Metals Reference Book,* Ch. 13, Elsevier Science & Technology, (2003).

14.   A.R. Paul, K.N.G. Kaimal, M.C. Naik, S.R. Dharwadkar, "Lattice and grain boundary diffusion of chromium in superalloy Incoloy-800," *Journal of Nuclear Materials,* **217**, 75-81 (1994).

15.   T. Ericsson, "A Study of the Cr-Depleted Surface Layers Formed on Four Cr-Ni Steels During Oxidation in Steam at 600°C and 800°C," *Oxidation of Metals,* **2**, 401-417 (1970).

16.   W. Wu, S. Guo, J. Zhang, "Exchange Current Densities and Charge-Transfer Coefficients of Chromium and Iron Dissolution in Molten LiF-NaF-KF Eutectic," *Journal of The Electrochemical Society*, **164**, C840-C844 (2017).